9 WARPED EXTRA DIMENSIONS AND THE RANDALL-SUNDRUM MODEL

9.1 Introduction

JoAnne L. Hewett and Thomas G. Rizzo

The Randall-Sundrum (RS) model of localized gravity [1] offers a potential solution to the hierarchy problem that can be tested at present and future accelerators [2, 3]. In the original (and most simple) version of this model, all of the Standard Model (SM) fields are confined to one of two branes that are sited at the S_1/Z_2 orbifold fixed points embedded in a 5-dimensional anti-de Sitter space (AdS$_5$). The theory is described by the metric $ds^2 = e^{-2k|y|}\eta_{\mu\nu}dx^\mu dx^\nu - dy^2$, with y being the extra dimension and where r_c is the compactification radius; thus the two branes are separated by a distance πr_c. The parameter k characterizes the curvature of the 5-dimensional space and is naturally of order the Planck scale. The two branes form the boundaries of the AdS$_5$ slice and gravity is localized on the Planck brane located at $y = 0$. Mass parameters on the TeV brane, located at $y = r_c\pi$, are red-shifted compared to those on the $y = 0$ brane and are typically given by $\Lambda_\pi = \overline{M}_{Pl}e^{-kr_c\pi}$, where $\overline{M}_{Pl}$ is the reduced Planck scale. In order to address the hierarchy problem, $\Lambda_\pi \sim$ TeV and hence the separation between the two branes, r_c, must have a value of $kr_c \sim 11 - 12$. It has been [4] demonstrated that this quantity can be naturally stabilized to this range of values.

There are very many variations on this basic model mostly having to do with placing at least some of the SM fields into the bulk for model building purposes [5–8]. In many cases it is also useful to include brane kinetic terms for these fields [9–15] to increase model flexibility. In almost all cases where a fundamental Higgs field is present it remains on the TeV brane (without Kaluza-Klein (KK) excitations) even when fermion and gauge fields are in the bulk. Up until recently this was thought to be necessary to avoid fine-tuning and phenomenological requirements. It has recently been shown that the fundamental Higgs can also be a bulk field [16, 17] which can lead to significant changes in Higgs phenomenology.

9.1.1 Graviton phenomenology

Since in all cases the graviton is a bulk field in 5-d we not only have the familiar zero mode massless graviton but also the massive tower of Kaluza-Klein excitations. The wavefunctions of these states in the extra dimension (in this simple version of the model) are given by

$$\chi_n = \frac{e^{2\sigma}}{N_n}J_2\Big(x_n\epsilon e^\sigma\Big), \tag{9.1}$$

with J_2 the usual Bessel function, $\sigma = k|y|$ and N_n a normalization factor. The KK graviton masses are given by $m_n = x_n k\epsilon$ with $\epsilon = e^{-\pi kr_c} \simeq 10^{-16}$, while the x_n roots can be obtained from the equation

$$J_1(x_n) = 0. \tag{9.2}$$

The wavefunction of the ordinary massless graviton is flat. Note that since $k\epsilon \sim$ TeV, the graviton KK excitations are TeV-scale.

In this simplest scenario, the graviton KK phenomenology is governed by 2 parameters, $k/\overline{M}_{Pl}$ and m_1 (or Λ_π). The action is computed by performing a linear expansion of the flat metric $g_{AB} = e^{-2ky}(\eta_{AB} + 2h_{AB}/M_5^{3/2})$, which for this scenario includes the warp factor. The interactions of the graviton KK tower with the SM fields on the TeV-brane are given by

$$\mathcal{L} = -\frac{1}{\overline{M}_{Pl}}T^{\mu\nu}(x)h_{\mu\nu}^0(x) - \frac{1}{\Lambda_\pi}T^{\mu\nu}(x)\sum_{n=1}^{\infty}h_{\mu\nu}^{(n)}(x), \tag{9.3}$$

where $T^{\mu\nu}$ is the conserved stress-energy tensor. The zero-mode decouples and the couplings of the excitation states are inverse-TeV strength. The hallmark signature for this scenario [2] is the presence of
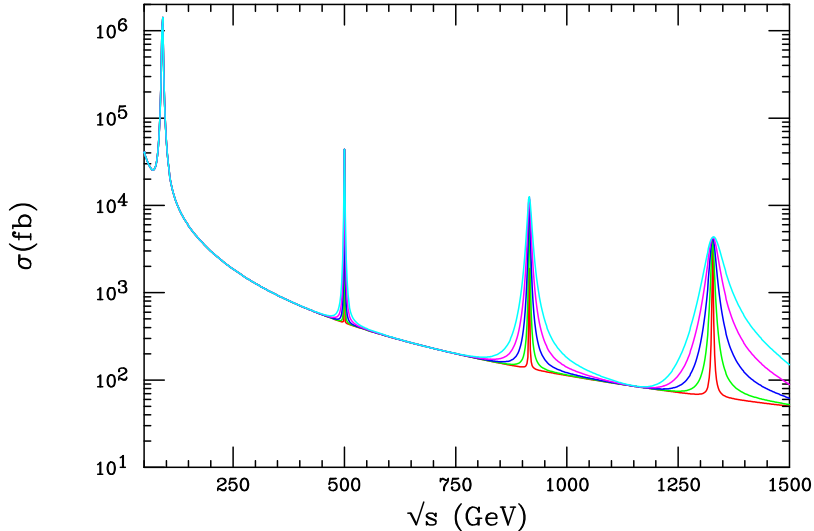
Fig. 9.1: The cross section for $e^+e^- \to \mu^+\mu^-$ including the exchange of a KK tower of gravitons in the RS model with $m_1 = 500$ GeV. The various curves correspond to $k/\overline{M}_{Pl}$ in the range $0.01 - 0.1$. From [2].

TeV-scale spin-2 graviton resonances at colliders; the KK spectrum in $e^+e^- \to \mu^+\mu^-$, taking $m_1 = 500$ GeV, is shown in Fig. 9.1. Note that the curvature parameter controls the width of the resonance. The LHC can discover these resonances in the Drell-Yan channel if $\Lambda_\pi < 10$ TeV [3], provided that the resonance width is not too narrow, and determine their spin-2 nature via the angular distributions of the final-state lepton pairs [18] if enough statistics are available. This is illustrated in Fig. 9.2 which displays the LHC search reach and the present experimental and theoretical constraints on the RS parameter space.

If the KK gravitons are too massive to be produced directly, their contributions to fermion pair production may still be felt via virtual exchange. In this case, the uncertainties associated with a cut-off (as present in the large extra dimensions scenario) are avoided, since there is only one additional dimension and thus the KK states may be neatly summed. The resulting sensitivity to the scale Λ_π at the LHC is $\Lambda_\pi = 3.0 - 20.0$ TeV as k varies in the range $k/\overline{M}_{Pl} = 0.01 - 1.0$. The 1 TeV International Linear Collider extends this reach by a factor of $1.5 - 2$.

Extensions of this simplest scenario modify the graviton KK spectrum and couplings. If the SM fields are allowed to propagate in the bulk, then each SM state also expands into a KK tower. The couplings of the bulk SM fields to the graviton KK states are cataloged in [3], where it is shown that the zero-mode fermion and gauge couplings to the graviton KK excitations are substantially reduced compared to the case where the SM fields are constrained to the TeV-brane. Graviton searches can then become more difficult in this scenario and are highly dependent on the explicit localization of the SM fields in the 5th dimension.

The inclusion of brane kinetic terms, which arise from higher order effects, also alter the graviton KK phenomenology [10]. The graviton KK masses are again given by $m_n = x_n \Lambda_\pi k/\overline{M}_{Pl}$, where the x_n are now roots of the equation $J_1(x_n) - \gamma_\pi x_n J_2(x_n) = 0$. Here, γ_π represents the coefficient of the boundary term for the TeV-brane and is naturally of order unity. The couplings are modified to be

$$\mathcal{L} = -\frac{1}{\overline{M}_{Pl}} T^{\mu\nu}(x) h^0_{\mu\nu}(x) - \frac{1}{\Lambda_\pi} T^{\mu\nu}(x) \sum_{n=1}^{\infty} \lambda_n h^{(n)}_{\mu\nu}(x), \qquad (9.4)$$

where λ_n depends on the coefficient of the boundary terms on both branes. This yields a dramatic reduction of the graviton KK couplings to SM fields on the TeV-brane, even for small values of the brane kinetic term coefficients. The resulting degradation in the graviton search reach at the LHC is displayed in Fig 9.3 for 100 fb^{-1} of integrated luminosity. From this figure, it is clear that the LHC can no longer
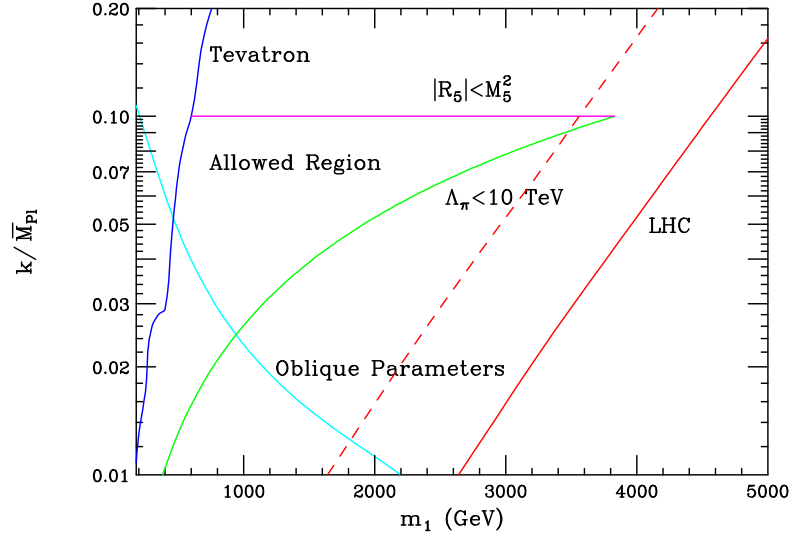
Fig. 9.2: Summary of experimental and theoretical constraints on the RS model in the two-parameter plane $k/\overline{M}_{Pl} - m_1$. The allowed region lies in the center. From [3].

cover all of the interesting parameter space for this model. For example, a first graviton KK excitation of mass 600 GeV with $k/\overline{M}_{Pl} = 0.01$ may still miss detection.

From a theoretical perspective, the RS model may be viewed as an effective theory whose low energy features originate from a full theory of quantum gravity, such as string theory. One may thus expect that a more complete version of this scenario admits the presence of additional dimensions compactified on a manifold $\mathcal{M}^\delta$ of dimension δ. The existence of an extra manifold also modifies the conventional RS phenomenology and collider signatures [19]. For the simplest scenario of an additional S^1 manifold, the RS metric is expanded to $ds^2 = e^{-2kr_c\phi}\eta_{\mu\nu}dx^\mu dx^\nu + r_c^2 d\phi^2 + R^2 d\theta^2$, where θ parameterizes the S^1, and R represents its radius. The masses of the KK states are now given by $m_{n\ell} = x_{n\ell}\Lambda_\pi k/\overline{M}_{Pl}$, where the $x_{n\ell}$ are solutions of the equation $2J_\nu(x_{n\ell}) + x_{n\ell}J'_\nu(x_{n\ell}) = 0$, with $\nu \equiv \sqrt{4 + (\ell/kR)^2}$. The KK mode number ℓ corresponds to the orbital excitations, while n denotes the usual RS AdS_5 mode levels. The couplings of the $m_{n\ell}$ graviton KK states are then given by

$$\mathcal{L} = -\frac{1}{\overline{M}_{Pl}}T^{\mu\nu}(x)h^0_{\mu\nu}(x) - \frac{1}{\Lambda_\pi}T^{\mu\nu}(x)\sum_{n=1}^{\infty}\xi(n\ell)h^{(n,\ell)}_{\mu\nu}(x)\,, \tag{9.5}$$

where $\xi(n\ell)$ depends on k, R, and $x_{n\ell}$ [19]. In particular, the addition of the S^δ background to the RS setup results in the emergence of a forest of graviton KK resonances. These originate from the orbital excitations on the S^δ and occur in between the original RS resonances. A representative KK spectrum is depicted in Fig. 9.3 for the additional S^1 manifold.

Finally, we note that the graviton KK spectrum and couplings to matter fields on the TeV brane will be modified if higher curvature terms are present in the action [20].

9.1.2 Radion basics

Fluctuations about the stabilized RS configuration allow for two massless excitations described by the metric tensor. The first of these corresponds to the usual graviton as discussed above while the second is a new scalar field essentially arising from the $\sim g_{55}$ component of the 5-d metric and is known as the radion (ϕ_0). Recall that when the 5-d graviton field is decomposed into 4-d fields it consists of a tower of tensor fields $\sim g_{\mu\nu}$ in addition to a tower of vectors $\sim g_{5\mu}$ and a tower of scalars $\sim g_{55}$. When the graviton KK fields acquire mass by eating the corresponding vector and scalar fields. With the orbifold
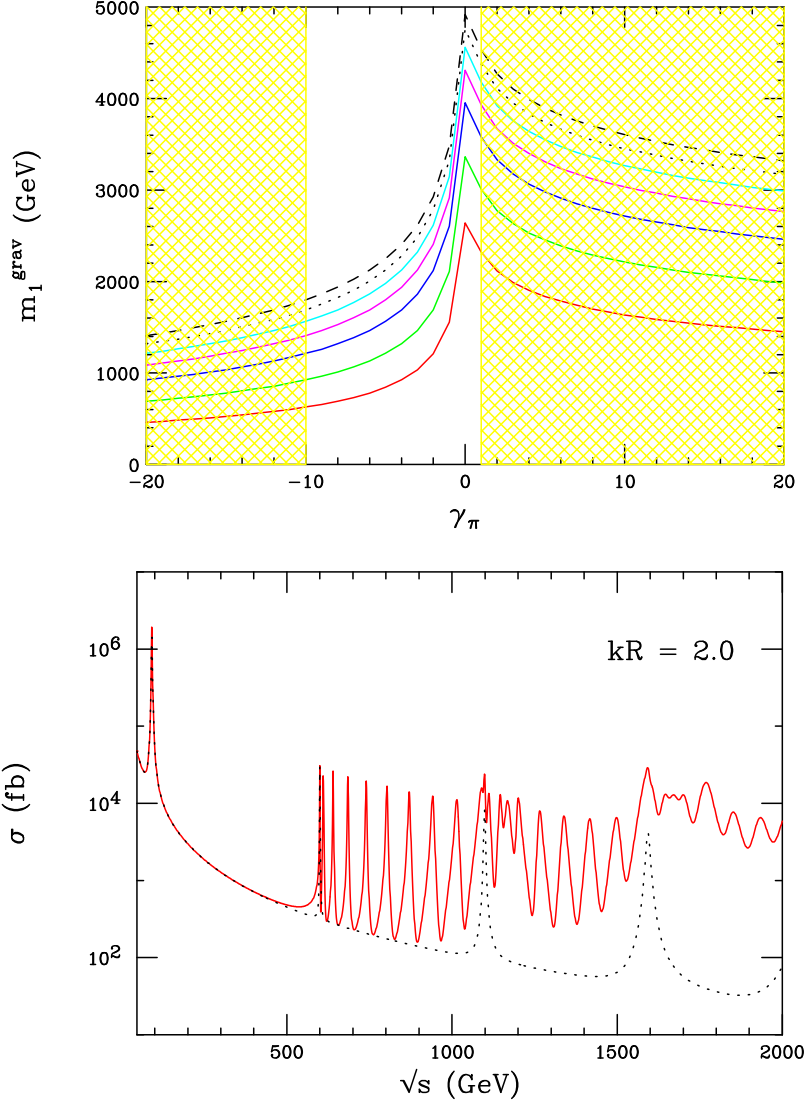
Fig. 9.3: Top: Search reach for the first graviton KK resonance employing the Drell-Yan channel at the LHC with an integrated luminosity of $100\,fb^{-1}$ as a function of the boundary term coefficient γ_π assuming $\gamma_0 = 0$. From bottom to top on the RHS of the plot, the curves correspond to $k/\overline{M}_{Pl} = 0.01, 0.025, 0.05, 0.075, 0.10, 0.125$ and 0.15, respectively. The unshaded region is that allowed by naturalness considerations and the requirement of a ghost-free radion sector. From [10]. Bottom: The solid (red) curve corresponds to the cross section for $e^+e^- \to \mu^+\mu^-$ when the additional dimension is orbifolded, i.e., for S^1/Z_2, with $m_{10} = 600$ GeV, $k/\overline{M}_{Pl} = 0.03$ and $kR = 2.0$. The result for the conventional RS model is also displayed, corresponding to the dotted curve. From [19].

symmetry imposed only a massless graviton and radion remain. This scalar radion field corresponds to a quantum excitation of the separation between the two branes. The mass of the radion is proportional to the backreaction of the bulk scalar vacuum expectation value (vev) on the metric and is correlated with the stabilization mechanism.

Generally, one expects that the radion mass should be in the range of a few $\times 10\,\text{GeV} \leq m_{\phi_0} \leq \Lambda_\pi$, where the lower limit arises from radiative corrections and the upper bound is the cutoff of the effective field theory. The radion mass m_{ϕ_0} is then expected to be below the scale Λ_π implying that the radion may be the lightest new field present in the RS model. A basic introduction to the radion and its origins can be found in [21, 22] while some basic phenomenology can be found in [23–25].

Unlike the graviton which couples directly to the stress-energy tensor, T_ν^μ, as seen above, the radion's couplings to SM matter fields on the TeV brane are proportional to the trace of the stress tensor, T_μ^μ:

$$\mathcal{L}_{eff} = -\frac{\phi_0(x)\,T_\mu^\mu}{\sqrt{6}\Lambda_\pi}\,. \tag{9.6}$$

These simplified couplings can be modified by the existence of brane kinetic terms for the graviton [10, 16] as well as when SM fields are placed in the bulk. The explicit couplings of the (unmixed) radion to SM fields are qualitatively similar to that of the Higgs, e.g., for fermions and massive gauge bosons we have

$$\mathcal{L} = \frac{1}{v}\gamma(m_f \bar{f}f - m_V^2 V_\mu V^\mu)\phi_0\,, \tag{9.7}$$

where v is the SM Higgs vev and γ is the ratio

$$\gamma = \frac{v}{\sqrt{6}\Lambda_\pi}\,, \tag{9.8}$$

which we might expect to be of order a few percent. The corresponding coupling to gluon pairs occurs through the trace anomaly and can be written as

$$\mathcal{L} = c_g^0 \frac{\alpha_s}{8\pi} G_{\mu\nu} G^{\mu\nu} \phi_0\,, \tag{9.9}$$

with

$$c_g^0 = \frac{1}{2v}\gamma[F_g - 2b_3]\,. \tag{9.10}$$

Here $b_3 = 7$ is the $SU(3)$ β-function and F_g is a well-known kinematic loop-function [26] of the ratio of masses of the top-quark to the radion while the second term originates from the anomaly. Similarly the radion coupling to two photon pairs is now given by

$$\mathcal{L} = c_\gamma^0 \frac{\alpha_{em}}{8\pi} F_{\mu\nu} F^{\mu\nu} \phi_0\,, \tag{9.11}$$

where

$$c_\gamma^0 = \frac{1}{v}\gamma[F_\gamma - (b_2 + b_Y)]\,. \tag{9.12}$$

Here, $b_2 = 19/6$ and $b_Y = -41/6$ are the $SU(2) \times U(1)$ β-functions and F_γ is another well-known kinematic function [26] of the ratios of the W boson and top-quark masses to the radion and the second term again originates from the trace anomaly.

9.1.3 Radion-Higgs mixing

Since the radion and Higgs are both real scalar fields they might mix. In fact such a mixing can proceed through a dimension-4 brane term when there is a single Higgs doublet on the TeV brane, through an interaction term of the form

$$S_{rH} = -\xi \int d^4x \sqrt{-g_{ind}} R^{(4)}[g_{ind}] H^\dagger H\,. \tag{9.13}$$

Here H is the Higgs doublet field, $R^{(4)}[g_{ind}]$ is the 4-d Ricci scalar constructed out of the induced metric g_{ind} on the SM brane, and ξ is a dimensionless mixing parameter assumed to be of order unity (since there is no reason why such an operator should be suppressed) and with unknown sign. We note that the structure of this mixing is quite different when the Higgs field is in the bulk [16]. In any case, such an interaction term leads to both gauge kinetic and mass mixing between the unmixed Higgs, h_0, and the radion.

The resulting Lagrangian can be diagonalized by a set of field redefinitions and rotations [22]

$$
\begin{aligned}
h_0 &= Ah + B\phi \,, \\
\phi_0 &= Ch + D\phi \,,
\end{aligned}
\tag{9.14}
$$

with

$$
\begin{aligned}
A &= \cos\theta - 6\xi\gamma/Z \sin\theta \,, \\
B &= \sin\theta + 6\xi\gamma/Z \cos\theta \,, \\
C &= -\sin\theta/Z \,, \\
D &= \cos\theta/Z \,,
\end{aligned}
\tag{9.15}
$$

where h, ϕ represent the physical, mass-eigenstate fields, and

$$
Z^2 = 1 + 6\xi(1 - 6\xi)\gamma^2 \,,
\tag{9.16}
$$

The factor Z serves to bring the physical radion kinetic term to canonical form and as such it must satisfy $Z > 0$ to avoid ghosts. For a fixed value of γ this implies that the range of ξ is bounded, i.e., $\xi_- \leq \xi \leq \xi_+$, where

$$
\xi_\pm = \frac{1}{12}[1 \pm (1 + 4/\gamma^2)^{1/2}] \,,
\tag{9.17}
$$

For example, if γ takes on the natural values, e.g., $\gamma = 0.1$ then ξ must lie in the approximate range $-1.585 \leq \xi \leq 1.752$. The masses of the physical states, ϕ, h, are then given by

$$
m_\pm^2 = \frac{1}{2}\Big[T \pm \sqrt{T^2 - 4F}\,\Big] \,,
\tag{9.18}
$$

where $m_+(m_-)$ is the larger(smaller) of the two masses and

$$
\begin{aligned}
T &= (1 + t^2)m_{h_0}^2 + m_{\phi_0}^2/Z \,, \\
F &= m_{h_0}^2 m_{\phi_0}^2/Z^2 \,,
\end{aligned}
\tag{9.19}
$$

with m_{h_0,ϕ_0} being the weak interaction eigenstate masses and $t = 6\xi\gamma/Z$. This mixing will clearly affect the phenomenology of both the radion and Higgs fields, for example, the bounds on the Higgs mass from LEP searches. Here, we note the modifications to the properties of the Higgs boson, in particular its decay widths and branching fractions, induced by this mixing and find that substantial differences from the SM expectations for the Higgs can be obtained. In the case where the Higgs is in the bulk a general procedure similar to the above can be followed to get to the mass eigenstate basis [16]. The main difference, in addition to the existence of the Higgs KK tower (all of whose members now mix with the radion), is that the Higgs-radion mixing term now occurs both in the bulk as well as on both branes.

9.2 Higgs–radion phenomenology

Daniele Dominici and John F. Gunion

The main consequence of Higgs-radion mixing is a modification of the prospects for discovering a light Higgs boson at the LHC [23, 25, 27]. In particular, this mixing could suppress or enhance the signal rate in the channel $gg \to H \to \gamma\gamma$. The effect of this mixing has been studied [25] by implementing the new Higgs and radion couplings in the HDECAY program [28]. Let us first recall the parameters of the model: when the mixing parameter $\xi \neq 0$, there are four independent parameters that must be specified to fix the mixing coefficients A, B, C, D (d, c, a, b in the notation of [25]) defining the mass eigenstates, h and ϕ, in terms of the unmixed Higgs and radion states, h^0 and ϕ^0. These are

$$\xi, \quad \Lambda_\phi = \sqrt{6}\Lambda_\pi, \quad m_h, \quad m_\phi, \tag{9.20}$$

where m_h and m_ϕ denote the eigenstate masses of the Higgs and of the radion, defined so that $h \to h^0$ and $\phi \to \phi^0$ in the $\xi \to 0$ limit. An additional parameter is required to determine the phenomenology of the scalar sector, including all possible decays: the mass, m_1, of the first KK graviton excitation.

Let us first review how the most relevant Higgs decays are modified. In Fig. 9.4, we plot the branching ratios for $h \to b\bar{b}$, gg, WW^*, ZZ^* and $\gamma\gamma$ as a function of the mixing parameter ξ, taking $m_h = 120$ GeV and $\Lambda_\phi = 5$ TeV. Results are shown for three different m_ϕ values: 20, 55 and 200 GeV. These plots are limited to ξ values allowed by the theoretical and experimental constraints [25]. Large values for the gg branching ratio, due to the anomalous contribution to the hgg coupling, suppress the other branching ratios to some extent. The anomalous contribution to the $h\gamma\gamma$ coupling is less important due to presence of the large W loop contribution in this case. Second, for $m_\phi = 55$ GeV, $BR(h \to \phi\phi)$ is large at large $|\xi|$ and suppresses the conventional branching ratios. For larger $|\xi|$, the changes in the branching ratio of the h with respect to the SM are at a level that would be observable, often at the LHC but with greatest certainty at the ILC. In addition, the anomalous contribution to the ggh coupling implies substantial changes in the $gg \to h$ production rate at the LHC.

The above results imply that detection of the h at the LHC could be significantly modified if $|\xi|$ is large. To illustrate this, we plot in Fig. 9.5 the ratio of the rates for $gg \to h \to \gamma\gamma$, $WW \to h \to \tau^+\tau^-$ and $gg \to t\bar{t}h \to t\bar{t}b\bar{b}$ (the latter two ratios being equal) to the corresponding rates for the SM Higgs boson. For this figure, we take $m_h = 120$ GeV and $\Lambda_\phi = 5$ TeV and show results for $m_\phi = 20$, 55 and 200 GeV. The result is that prospects for h discovery in the $gg \to h \to \gamma\gamma$ and $WW \to h \to \tau^+\tau^-$ modes could be either substantially poorer or substantially better than for a SM Higgs boson of the same mass, depending on ξ and m_ϕ.

For $m_\phi > m_h$, the suppression is very substantial for large, negative values of ξ. This region of significant suppression becomes wider at large values of m_ϕ and Λ_ϕ. In contrast, for $m_\phi < m_h$, the $gg \to h \to \gamma\gamma$ rate is generally only suppressed when $\xi > 0$. All this is shown, in a quantitative way, by the contours in Fig. 9.6 [29]. The outermost, hourglass shaped contours define the theoretically allowed region. Three main regions of non-detectability may appear. Two are located at large values of m_ϕ and $|\xi|$. A third region appears at low m_ϕ and positive ξ, where the above-noted $gg \to h \to \gamma\gamma$ suppression sets in. It becomes further expanded when $2m_\phi < m_h$ and the decay channel $h \to \phi\phi$ opens up, thus reducing the $h \to \gamma\gamma$ branching ratio. These regions shrink as m_h increases, since additional channels, in particular $gg \to h \to ZZ^* \to 4\ell$, become available for Higgs discovery. At $m_h = 120$ GeV, these regions are reduced by considering either a larger data set or qqh Higgs production, in association with forward jets. An integrated luminosity of 100 fb^{-1} would remove the regions of non-detection shown in Fig. 9.6 at large positive ξ in the case of $\Lambda_\phi = 5$ TeV. Similarly, including the $qqh, h \to WW^* \to \ell\ell\nu\bar{\nu}$ channel in the list of the discovery modes removes the same two regions and reduces the large region of h non-observability at negative ξ values. In all these regions, a complementarity is potentially offered by the process $gg \to \phi \to ZZ^* \to 4\ell$, which becomes important for $m_\phi > 140$ GeV. At the LHC, this process would have the same event structure as the golden SM

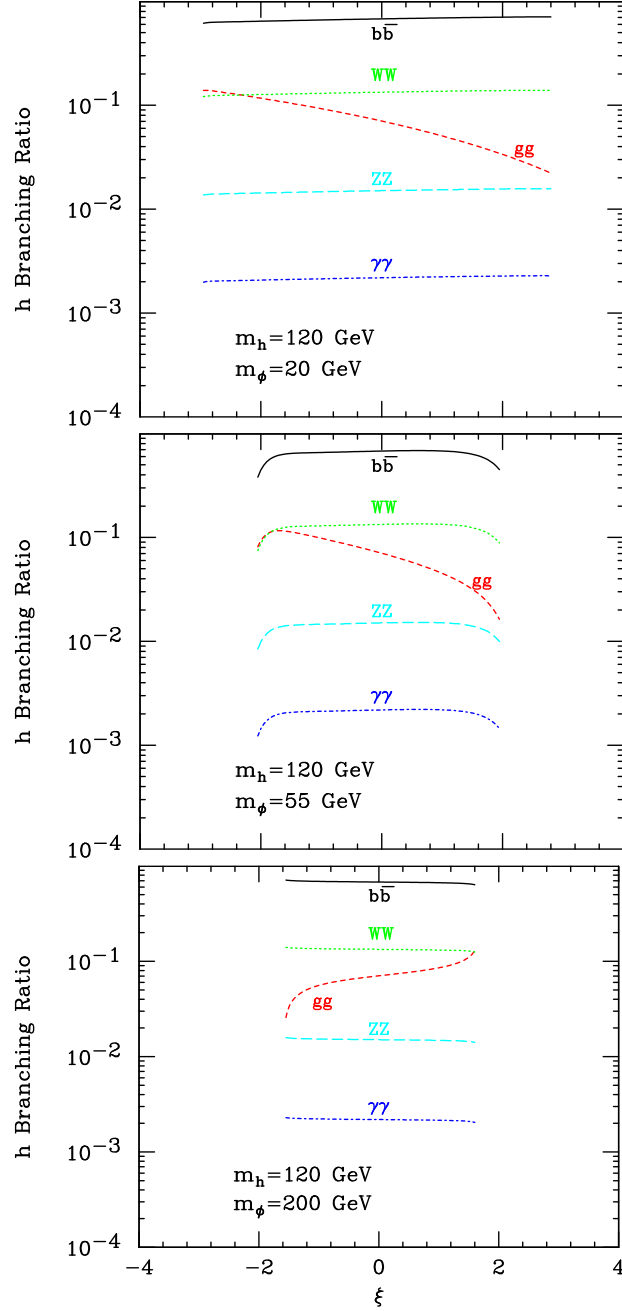Fig. 9.4: The branching ratios for h decays to $b\bar{b}$, gg, WW^*, ZZ^* and $\gamma\gamma$ for $m_h = 120$ GeV and $\Lambda_\phi = 5$ TeV as functions of ξ for $m_\phi = 20$, 55 and 200 GeV.

Higgs mode, $H \rightarrow ZZ^* \rightarrow 4\,\ell$, which has been thoroughly studied for an intermediate mass Higgs boson. By computing the $gg \rightarrow \phi \rightarrow ZZ^* \rightarrow 4\,\ell$ rate relative to that for the corresponding SM H process and employing the LHC sensitivity curve for $H \rightarrow ZZ^*$ of [30], the significance for the ϕ signal in the $4\,\ell$ final state at the LHC can be extracted. Results are overlayed on Fig. 9.6 assuming 30 fb^{-1} of data.

The observability of ϕ production in the four lepton channel fills most of the gaps in (m_ϕ, ξ) parameter space in which h detection is not possible (mostly due to the suppression of the loop-induced $gg \rightarrow h \rightarrow \gamma\gamma$ process). For example, for $\Lambda_\phi = 5$ TeV and $L = 30$ fb^{-1}, the observation of at least one scalar is guaranteed over almost the full parameter phase space, with the exception of: (a) the region
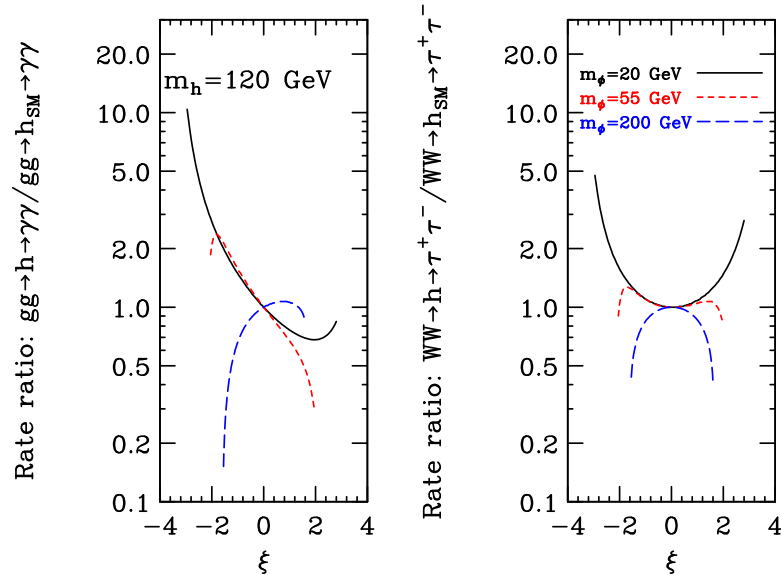
Fig. 9.5: The ratio of the rates for $gg \to h \to \gamma\gamma$ and $WW \to h \to \tau^+\tau^-$ (the latter is the same as that for $gg \to t\bar{t}h \to t\bar{t}b\bar{b}$) to the corresponding rates for the SM Higgs boson. Results are shown for $m_h = 120$ GeV and $\Lambda_\phi = 5$ TeV as functions of ξ for $m_\phi = 20, 55$ and 200 GeV.

of large positive ξ with $m_\phi < 120$ GeV, where the $\phi \to ZZ^*$ decay is phase-space-suppressed; and (b) a narrow region with $\xi < 0$ and $m_\phi \simeq 170$ GeV. The latter region arises due to the ramp-up of the $\phi \to W^+W^-$ channel; in this region a luminosity of order 100 fb^{-1} is required to reach a $\geq 5\sigma$ signal for $\phi \to ZZ^*$. We should also note that the $\phi \to ZZ$ decay is reduced for $m_\phi > 2m_h$ by the onset of the $\phi \to hh$ decay, which can become the main decay mode. The resulting $hh \to b\bar{b}b\bar{b}$ topology, with di-jet mass constraints, may represent a viable signal for the LHC in its own right [31, 32].

As seen in Fig. 9.6, there are regions of (m_ϕ, ξ) parameter space in which *both* the h and ϕ mass eigenstates will be detectable. In these regions, the LHC will observe two scalar bosons somewhat separated in mass with the lighter (heavier) having a non-SM-like rate for the gg-induced $\gamma\gamma$ (ZZ) final state. Despite the ability to see both eigenstates, still more information will be required to ascertain whether these two Higgs bosons derive from a multi-doublet or other type of extended Higgs sector or from the present type of model with Higgs-radion mixing [29].

The ILC should guarantee observation of both the h and the ϕ even in most of the regions within which detection of either at the LHC might be difficult. In particular, in the region with $m_\phi > m_h$ the hZZ coupling is enhanced relative to the SM HZZ coupling and h detection in e^+e^- collisions would be even easier than SM H detection. Further, assuming that e^+e^- collisions could also probe down to ϕZZ couplings of order $g^2_{\phi ZZ}/g^2_{HZZ} \simeq 0.01$, the ϕ would be seen in almost the entirety of the region for which ϕ detection at the LHC would not be possible. In this case, the measurements of the ZZ boson couplings of both the Higgs and the radion particles would significantly constrain the values of the ξ and Λ_ϕ parameters of the model. Furthermore, the ILC has the capability of extending the coupling measurements to all fermions separately with accuracies of order 1%-5% and achieves a determination of the total width to 4% - 6% accuracy [33]. This is shown in Fig. 9.7 by the additional contours, which indicate the regions where the discrepancy with the SM predictions for the Higgs couplings to pairs of b quarks and W bosons exceeds 2.5σ.

As already noticed, the presence in the Higgs radion sector of trilinear terms opens up the important possibility of $\phi \to hh$ decay and $h \to \phi\phi$. For example, for $m_h = 120$ GeV, $\Lambda_\phi = 5$ TeV and $m_\phi \sim 250 - 350$ GeV one finds $BR(\phi \to hh) \sim 0.2 - 0.3$. In [34], the CMS discovery potential for the radion in its two Higgs decay mode ($\phi \to hh$) with $\gamma\gamma + b\bar{b}$, $\tau\tau + b\bar{b}$ and $b\bar{b} + b\bar{b}$ final states was esti-
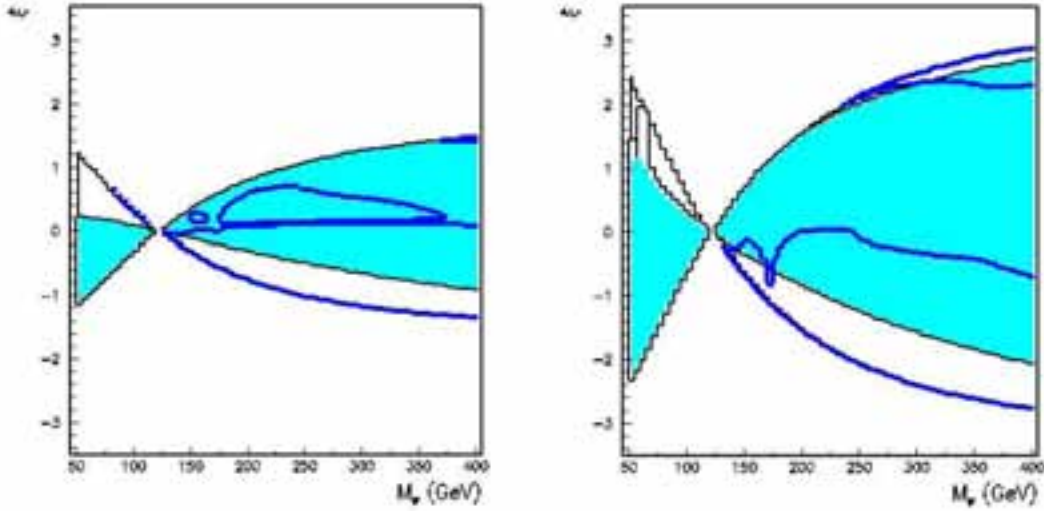
Fig. 9.6: Regions in (m_ϕ, ξ) parameter space of h detectability (including $gg \to h \to \gamma\gamma$ and other modes) and of $gg \to \phi \to ZZ^* \to 4\ell$ detectability at the LHC for one experiment and 30 fb^{-1}. The outermost, hourglass shaped contours define the theoretically allowed region. The light gray (cyan) regions show the part of the parameter space where the net h signal significance remains above 5σ. In the empty regions between the shading and the outermost curves, the net h signal drops below the 5σ level. The thick gray (blue) curves indicate the regions where the significance of the $gg \to \phi \to ZZ^* \to 4\ell$ signal exceeds 5σ. Results are presented for m_h=120 GeV and Λ_ϕ= 2.5 TeV (left), 5.0 TeV (right).
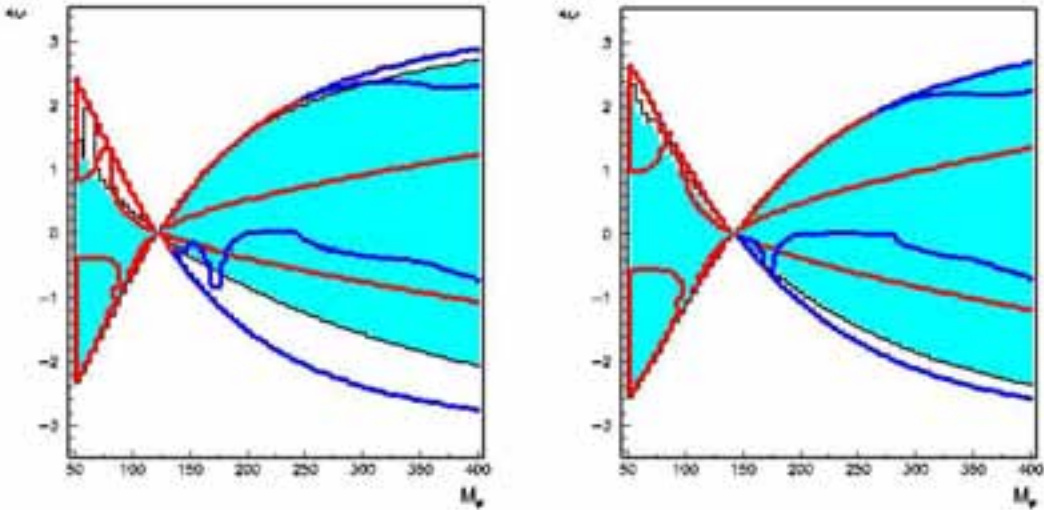

Fig. 9.7: Same as Fig. 9.6 for $m_h = 120$ GeV (left), 140 GeV (right) and $\Lambda_\phi = 5$ TeV with added contours, indicated by the medium gray (red) curves, showing the regions where the ILC measurements of the h couplings to $b\bar{b}$ and W^+W^- would provide a $> 2.5\sigma$ evidence for the radion mixing effect. (Note: the gray (red) lines are always present along the outer edge of the hourglass in the $m_\phi > m_h$ region, but are sometimes buried under the darker (blue) curves. In this region, the $> 2.5\sigma$ regions lie between the outer hourglass edges and the inner gray (red) curves.)

mated, assuming $m_h = 125$ GeV and $m_\phi = 300$ GeV. The $\gamma\gamma + b\bar{b}$ topology provides the best discovery potential. Details of this analysis and the corresponding analysis by ATLAS can be found respectively in Section 9.4 and Section 9.3.

9.3 Radion search in ATLAS

Georges Azuelos, Donatella Cavalli, Helenka Przysieniak and Laurent Vacavant

As explained in the introduction, the radion is a physical scalar that remains in 4-d from the 5-d metric tensor and from fluctuations about a stabilized Randall-Sundrum (RS) configuration. The presence of the radion is one of the important phenomenological consequences of theories of warped extra dimensions and observation of this scalar therefore constitutes a crucial probe of the model. This section summarizes the main results of a study performed for ATLAS [35].

The radion, being a scalar, has a Higgs-like phenomenology [21, 22, 36] but has large effective coupling to gluons. The decay branching ratios and widths depend on three parameters: the physical mass of the radion m_ϕ, the vacuum expectation value of the radion field, $\Lambda_\phi = \sqrt{6}\Lambda_\pi$ where Λ_π is the mass scale at the TeV brane in the RS model, and the radion-SM Higgs mixing parameter ξ.

Here, we have investigated the possibility of observing a RS radion with the ATLAS detector through the following decays: $\phi \to \gamma\gamma$, $\phi \to ZZ^{(*)} \to 4\ell$, $\phi \to hh \to b\bar{b}\gamma\gamma$ and $\phi \to hh \to b\bar{b}\tau^+\tau^-$. Only the direct production of the radion $gg \to \phi$ has been considered since it is the main process at LHC and it benefits from the enhancement of the coupling ϕgg.

9.3.1 $\phi \to \gamma\gamma$ and $ZZ^{(*)} \to 4\ell$

For the $\gamma\gamma$ ($m_\phi < 160$ GeV) and $ZZ^{(*)}$ ($m_\phi > 100$ GeV) decay channels, the radion signal significance is determined by reinterpreting the results from the SM Higgs analyses obtained with ATLAS [37], for 100 fb^{-1}. The ratio of the radion S/$\sqrt{\text{B}}$ over that of the SM Higgs is given by [21]:

$$\frac{\text{S}/\sqrt{\text{B}}\,(\phi)}{\text{S}/\sqrt{\text{B}}\,(h)} = \frac{\Gamma(\phi \to gg)\,\text{BR}(\phi \to \gamma\gamma,\,ZZ)}{\Gamma(h \to gg)\,\text{BR}(h \to \gamma\gamma,\,ZZ)} \sqrt{\frac{\max(\Gamma^h_{\text{tot}}, \sigma_m)}{\max(\Gamma^\phi_{\text{tot}}, \sigma_m)}} \tag{9.21}$$

where the σ_m are the experimentally reconstructed resonance widths for each of the two decay processes. The radion signal significance thus determined is shown as a function of the mass of the radion, in Fig. 9.8, for $\Lambda_\phi = 1, 10$ TeV, $\xi = 0, 1/6$, and for an integrated luminosity of 100 fb^{-1}.

9.3.2 $\phi \to hh \to \gamma\gamma b\bar{b}$

For the purpose of estimating the limits of observation of radion decay to a pair of SM Higgs bosons, two reference values are taken for the mass of the radion: 300 GeV and 600 GeV and a Higgs mass of 125 GeV (assumed to be known). The production cross sections in these cases are 58 pb and 8 pb respectively.

The specific decay channel $\phi \to hh \to \gamma\gamma b\bar{b}$ offers an interesting signature, with two high-p_T isolated photons and two b-jets. The background rate is expected to be very low for the relevant mass region $m_h > 115$ GeV and $m_\phi > 2m_h$. In addition, triggering on such events is easy and the diphoton mass provides very good kinematical constraints for the reconstruction of m_ϕ.

The backgrounds for this channel are $\gamma\gamma b\bar{b}$ (irreducible), $\gamma\gamma c\bar{c}$, $\gamma\gamma bj$, $\gamma\gamma cj$ and $\gamma\gamma jj$ (reducible with b-tagging). In the region of mass considered for the Higgs, the main production processes are the Born diagram $qq \to \gamma\gamma$ and the box diagram $gg \to \gamma\gamma$. The events were generated with PYTHIA [38] and some cuts had to be applied at the event generation: the sample was generated in seven different bins of $\hat{p}_\perp$, the transverse momentum defined in the rest frame of the hard interaction. Detector effects on the signal and background events were taken into account by the fast simulation code ATLFAST [39].
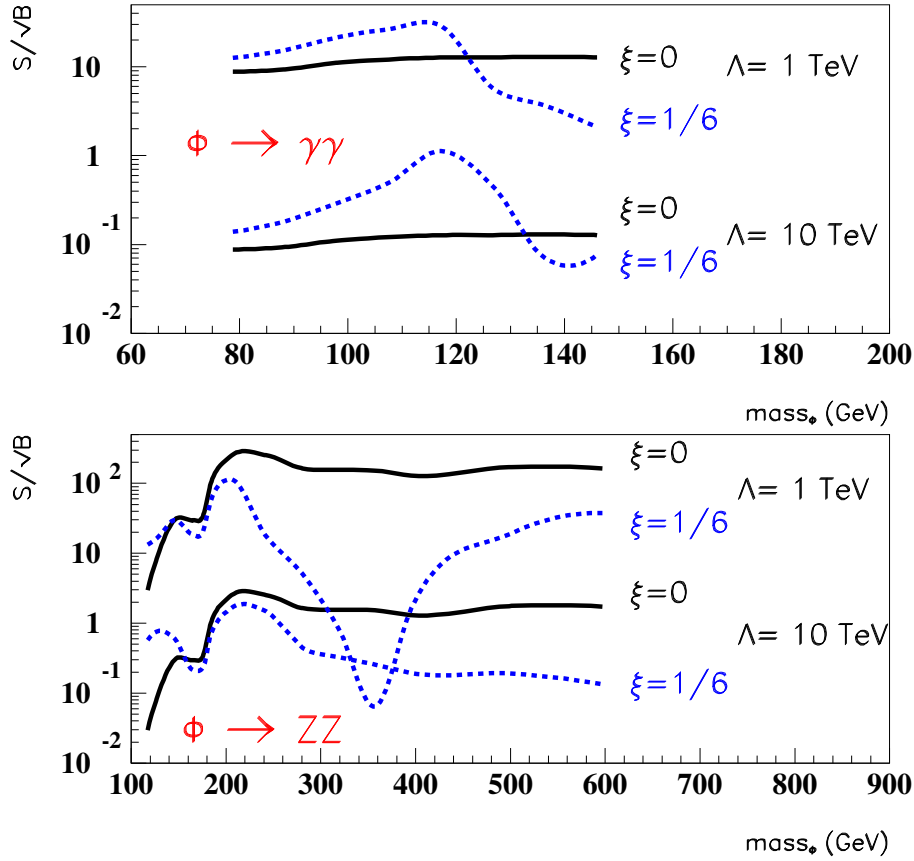
Fig. 9.8: Signal significance versus the mass of the radion, for the $\gamma\gamma$ channel (top) and for the $ZZ^{(*)}$ channel (bottom). In both plots, the values for $\Lambda_\phi = 1, 10$ TeV and $\xi = 0, 1/6$ are shown, for an integrated luminosity of 100 fb^{-1}.

To extract the signal, two isolated photons with $p_T > 20$ GeV and $|\eta| < 2.5$, and two jets with $p_T > 15$ GeV, $|\eta| < 2.5$ are required. At least one of the jets has to be tagged as a b. Fig. 9.9 shows the reconstructed radion mass for the case of $m_\phi = 300$ GeV and Table 9.1 shows the expected number of events for different cases of ξ and Λ_ϕ. The background is negligible. A few fb^{-1} would be sufficient to observe the radion if $\Lambda_\phi = 1$ TeV, and it is estimated that with 30 fb^{-1}, the reach in Λ_ϕ would be ~ 2.2 TeV for $m_\phi = 300$ GeV.

9.3.3 $\phi \to hh \to b\bar{b}\tau^+\tau^-$

The channel $\phi \to hh \to b\bar{b}\tau^+\tau^-$ provides another potentially interesting signal for radion discovery, although the background is higher and the reconstructed mass resolutions are poorer than in the $\phi \to hh \to \gamma\gamma b\bar{b}$ channel.

The background here are: $hh \to b\bar{b} \ \tau^+\tau^-$, $t\bar{t} \to bW^+ \ \bar{b}W^-$, Z +jets, followed by $Z \to \tau^+\tau^-$ and W + jets. In order to provide a trigger, a leptonic decay of one of the two τ's is required. Although the signal efficiency is low, the background rejection is high, after application of simple cuts (for details, see [35]). Figure 9.10 shows the reconstructed masses for signal when $m_\phi=300$ and 600 GeV respectively, for 30 fb^{-1}, $\Lambda_\phi = 1$ TeV and $\xi = 0$. The shape for a 300 GeV radion resonance is not distinguishable from the background (mostly $t\bar{t}$). Therefore systematic errors will most probably be dominated by the understanding of the level of this background.
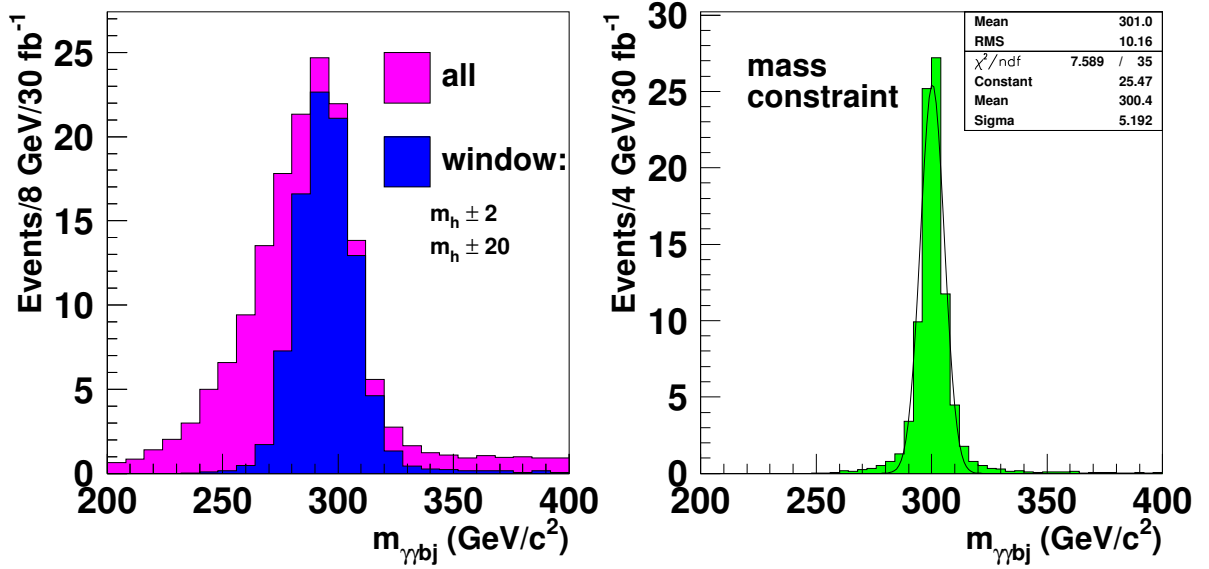
Fig. 9.9: Reconstructed $\gamma\gamma bj$ invariant mass distribution, for $m_\phi = 300$ GeV, $\xi = 0$, $\Lambda_\phi = 1$ TeV and for 30 fb^{-1}. The plots on the left show all combinations and the ones fulfilling the mass window cuts shown on the two Higgs resonances: $m_{\gamma\gamma} = m_h \pm 2$ GeV and $m_{bj} = m_h \pm 20$ GeV . The distribution on the right is obtained by constraining the reconstructed masses m_{bj} and $m_{\gamma\gamma}$ to the light Higgs mass m_h, after the mass window cuts.

	$m_\phi = 300$ GeV	$m_\phi = 600$ GeV
$\xi = 0, \Lambda_\phi = 1$ TeV	84.5	7.0
$\xi = 0, \Lambda_\phi = 10$ TeV	0.9	0.1
$\xi = 1/6, \Lambda_\phi = 1$ TeV	150.9	5.3
$\xi = 1/6, \Lambda_\phi = 10$ TeV	1.2	0.1

Table 9.1: Number of events selected for signal, $\phi \to hh \to \gamma\gamma b\bar{b}$ for $m_\phi =$ 300 and 600 GeV, for 30 fb^{-1} and for $m_h = 125$ GeV.
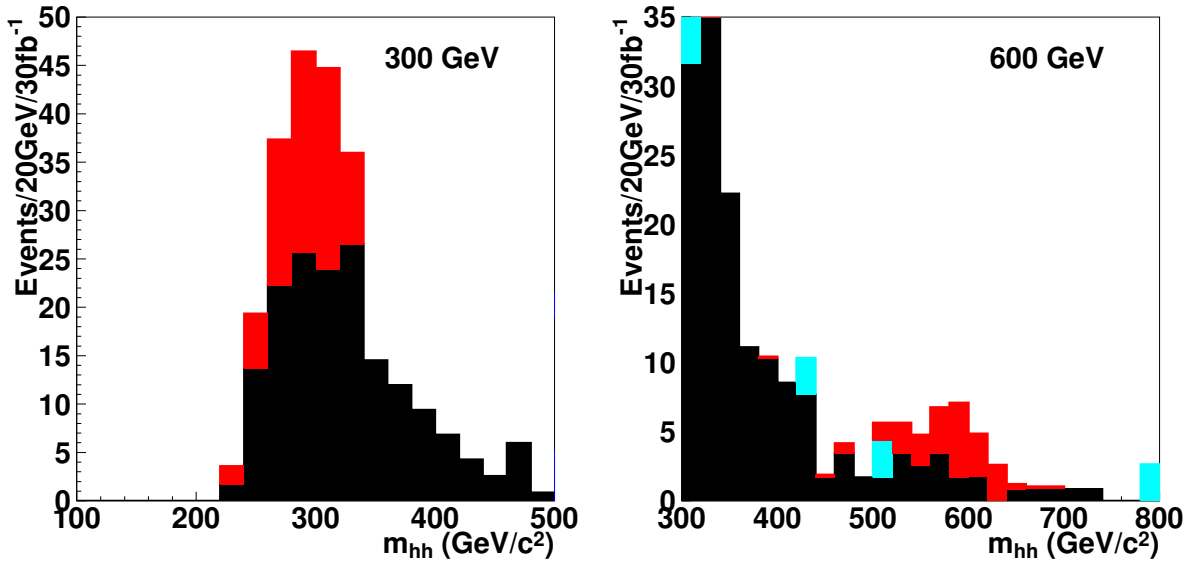
Fig. 9.10: Reconstructed mass of the radion, for 30 fb^{-1} and $\Lambda_\phi = 1$ TeV, $\xi = 0$. Left plot: expected signal (light) and $t\bar{t}$ background (dark). Right plot: $t\bar{t}$ background (dark), expected signal (light) and Z+jets background (very light).

Requiring a minimum of 10 events and $S/\sqrt{B} \geq 5$, the maximum reach in Λ_ϕ is 1.04 TeV for both m_ϕ=300 GeV and m_ϕ=600 GeV, but the uncertainties in background subtraction may affect considerably the observability of this channel in the first case.

9.3.4 Conclusions

The search for the radion at the LHC is similar to the case of the SM Higgs boson, and indeed the analyses already performed for the latter can be re-interpreted in terms of a radion search, after rescaling the branching ratios and widths. For an integrated luminosity of 100 fb^{-1}, the values $S/\sqrt{B} \sim 10$ (0.1) are obtained for the $\gamma\gamma$ channel, with a mixing parameter ξ=0 and a scale Λ_ϕ=1 (10) TeV, in the range 80 GeV $< m_\phi < 160$ GeV. For the $ZZ^{(*)}$ channel, $S/\sqrt{B} \sim 100$ (1) for 200 GeV $< m_\phi < 600$ GeV for the same conditions. Because the couplings are similar to those of the SM Higgs, a good measurement of the production cross section and branching ratios will be necessary to discriminate between the two scalars.

The radion can also decay into a pair of Higgs scalars, if the masses permit. Two cases were examined: $\phi \rightarrow hh \rightarrow \gamma\gamma b\bar{b}$ and $\phi \rightarrow hh \rightarrow \tau\tau b\bar{b}$, for radion masses of 300 and 600 GeV, for $m_h = 125$ GeV and for an integrated luminosity of 30 fb^{-1}. The maximal reach in Λ_ϕ is $\sim 1 - 2$ TeV. It must be remarked that a value of $\Lambda_\phi = 1$ TeV could be overly optimistic since, with the corresponding value of Λ_π and with a value of k/M_{Pl} even as large as 0.1, the mass of the first KK graviton state ($m_1 = 3.83(k/M_{Pl})\Lambda_\pi$) would be very low [40].

9.4 Radion search in CMS

Albert De Roeck, Guy Dewhirst, Daniele Dominici, Livio Fano, Simone Gennai and Alexander Nikitenko

The CMS discovery potential is estimated for the decay of the radion in a pair of Higgs bosons, with $\gamma\gamma b\bar{b}$, $\tau\tau b\bar{b}$ and $b\bar{b}b\bar{b}$ final states and for an integrated luminosity of 30 fb^{-1}. The study has been carried out for the radion mass of 300 GeV and the Higgs boson mass of 125 GeV . The sensitivity was evaluated
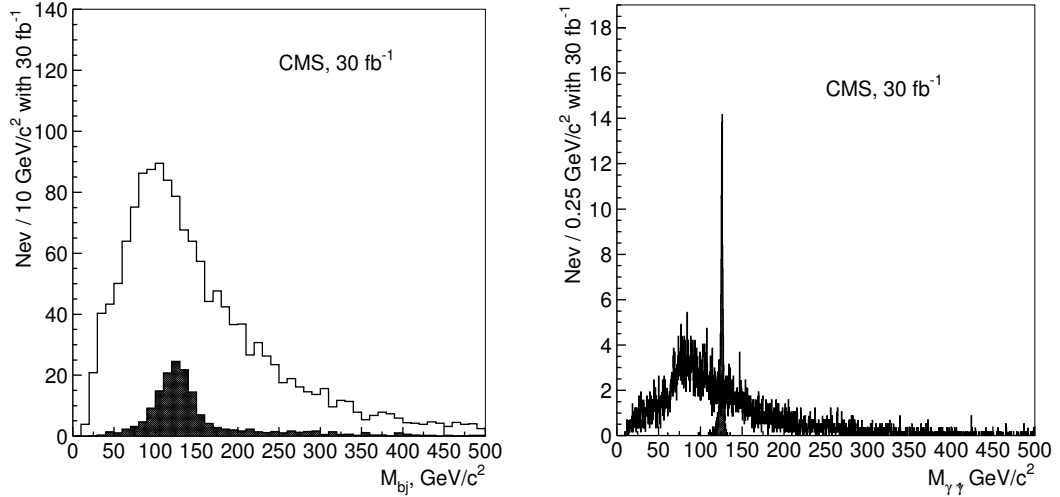
Fig. 9.11: The di-jet (left plot) and the di-photon (right plot) mass distribution for the background (open histogram) and the signal of $\phi \to hh \to \gamma\gamma b\bar{b}$ (full black histogram) after all selections except the mass window cuts with 30 fb^{-1}. The signal is shown for the maximal cross section times branching ratios point in (ξ-Λ_ϕ) plane.

in the (ξ,Λ_ϕ) plane, with systematics uncertainties included. A detailed description of the analysis can be found in [34]. A brief summary of the analysis and the results is presented below.

Signal events $gg \to \phi \to hh$ were generated with PYTHIA. The cross sections and branching ratios were evaluated using rescaled NLO cross sections for the SM Higgs boson and a modified HDECAY program. For the radion and Higgs boson mass points considered ($m_h = 125$ GeV, m_ϕ=300 GeV) and for Λ_ϕ= 1 TeV the maximal cross section times branching ratio is 71 fb for $\gamma\gamma b\bar{b}$ final state. For the $\tau\tau b\bar{b}$ final state with the topology considered in the analysis, one τ lepton decaying leptonically and the other τ lepton decaying hadronically (producing a τ jet), the maximal cross section times branching ratio is 960 fb. This maximal cross section is reached for the radion mixing parameter $\xi = -0.35$.

For the $\gamma\gamma b\bar{b}$ final state the irreducible backgrounds $\gamma\gamma jj (j = u, d, s, g)$ (generated with Com-pHEP) and the $\gamma\gamma c\bar{c}$ and $\gamma\gamma b\bar{b}$ (generated with MadGraph) were studied. The reducible background from γ+three jets and four-jet processes was not evaluated directly, but assumed to be the same as in for the inclusive $h \to \gamma\gamma$ analysis, namely 40% of the total background after all selection. For the $\tau\tau b\bar{b}$ final state, the $t\bar{t}$, Z+jets, W+jets backgrounds (generated with PYTHIA) and the $b\bar{b}Z$ background (generated with CompHEP) were studied.

9.4.1 The $\phi \to hh \to \gamma\gamma b\bar{b}$ channel

The $\gamma\gamma b\bar{b}$ events were required to pass the Level-1 and HLT di-photon trigger. In the off-line analysis two photon candidates with $E_T^{\gamma 1, \gamma 2} > 40, 25$ GeV were required to pass tracker cuts and calorimeter isolation cuts. Events with only two calorimeter jets of $E_T >$30 GeV and within $|\eta| <$2.4 were selected. At least one of these jets must be tagged as a b-jet. Finally, the di-photon mass, $M_{\gamma\gamma}$, was required to be in a window of ± 2 GeV, the di-jet mass, $M_{j\bar{b}}$, in a window of ± 30 GeV and the di-photon-di-jet mass, $M_{\gamma\gamma b\bar{b}}$, in a window ± 50 GeV around the Higgs and radion mass. Figure 9.11 shows the di-jet (left plot) and the di-photon (right plot) mass distribution for the background (open histogram) and the signal of $\phi \to hh \to \gamma\gamma b\bar{b}$ (full, black histogram) after all selections except the mass window cuts, and for 30 fb^{-1}. The signal is shown for the maximal cross section times branching ratios point in (ξ-Λ_ϕ) plane. Figure 9.12 (left plot) shows the $M_{\gamma\gamma bj}$ distribution for the background (dashed histogram) and for the signal of $\phi \to hh \to \gamma\gamma b\bar{b}$ plus background (solid histogram) after all selections, and for 30 fb^{-1}.
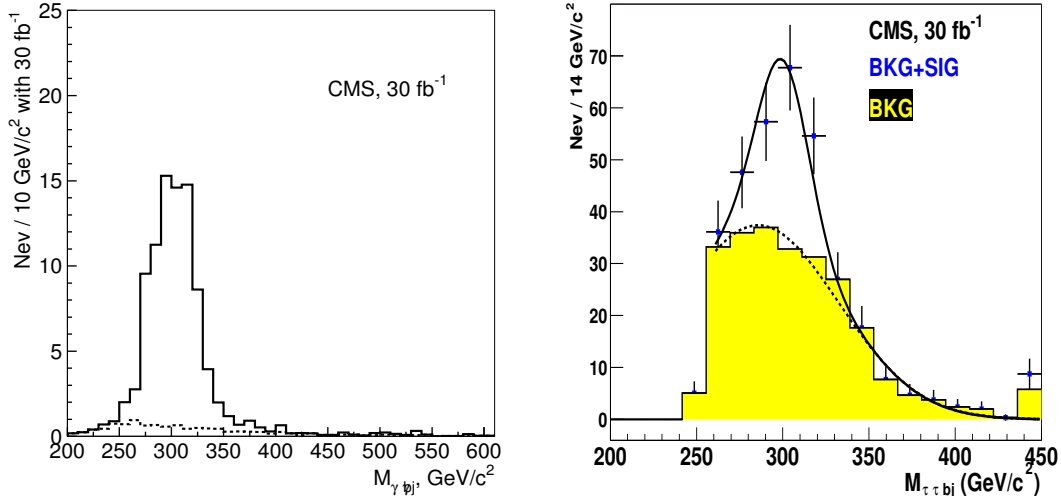
Fig. 9.12: Left plot: the $M_{\gamma\gamma bj}$ distribution for the background (dashed histogram) and for the signal of $\phi \rightarrow hh \rightarrow \gamma\gamma b\bar{b}$ plus background (solid histogram) after all selections for 30 fb^{-1}. Right plot: the $M_{\tau\tau bj}$ distribution for the background (full gray histogram) and for the signal of $\phi \rightarrow hh \rightarrow \tau\tau b\bar{b}$ plus background (black points with the error bars) after all selections for 30 fb^{-1}. The fitted curves for the background and signal plus background are superimposed. On both plots the signal is shown for the maximal cross section times branching ratios point in (ξ-Λ_ϕ)

9.4.2 The $\phi \rightarrow hh \rightarrow \tau\tau b\bar{b}$ channel

The $\tau\tau b\bar{b}$ events were selected by the single electron and muon triggers and by the combined e-plus-τ-jet and the μ-plus-τ-jet triggers. In the off-line analysis a lepton and τ-jet identification was performed. The requirements on the jets were similar to the ones used in the $\gamma\gamma b\bar{b}$ analysis. In addition a cut of the transverse mass of the lepton and missing transverse momentum, $M_T^{\ell\nu} < 35$ GeV was applied to suppress the $t\bar{t}$ and W+jets backgrounds. The di-τ-lepton mass was reconstructed using the missing transverse energy. The significance of the discovery was calculated using expected number of the signal and background events after the mass window selections: $100 < M_{bj} < 150$ GeV, $100 < M_{\tau\tau} < 160$ GeV and $280 < M_{\tau\tau} < 330$ GeV. Figure 9.12 (right plot) shows the $M_{\tau\tau bj}$ distribution for the background (full, gray histogram) and for the signal of $\phi \rightarrow hh \rightarrow \tau\tau b\bar{b}$ plus background (black points with the error bars) after all selections, for 30 fb^{-1}. Fitted curves for the background and the signal plus background are superimposed.

9.4.3 The $\phi \rightarrow hh \rightarrow b\bar{b}b\bar{b}$ channel

The four b-jet final state yields the highest rate for the signal. The maximal cross section times branching ratio at $\Lambda_\phi = 1$ TeV is 10.3 pb, which results in about 3.1×10^5 signal events for 30 fb^{-1}. The effective triggering and selection in the off-line analysis of the events is, however a big challenge due to the huge multi-jet background rate. In fact the remaining background is a few orders of magnitude larger that the signal in the relevant mass range. Techniques can be envisaged to normalize the background directly from a signal free region and predict the number of background events in the signal region. In order to make a 3σ discovery, such extrapolation needs to be performed with a precision of about 0.1%, making this channel essentially hopeless.

9.4.4 Results

The background contribution to the $\gamma\gamma b\bar{b}$ final state can be determined directly from the $\gamma\gamma$-plus-two-jets data obtained after all selections, except the final mass window cuts on the $M_{\gamma\gamma}$, $M_{j\bar{b}}$ and $M_{\gamma\gamma b\bar{b}}$. The
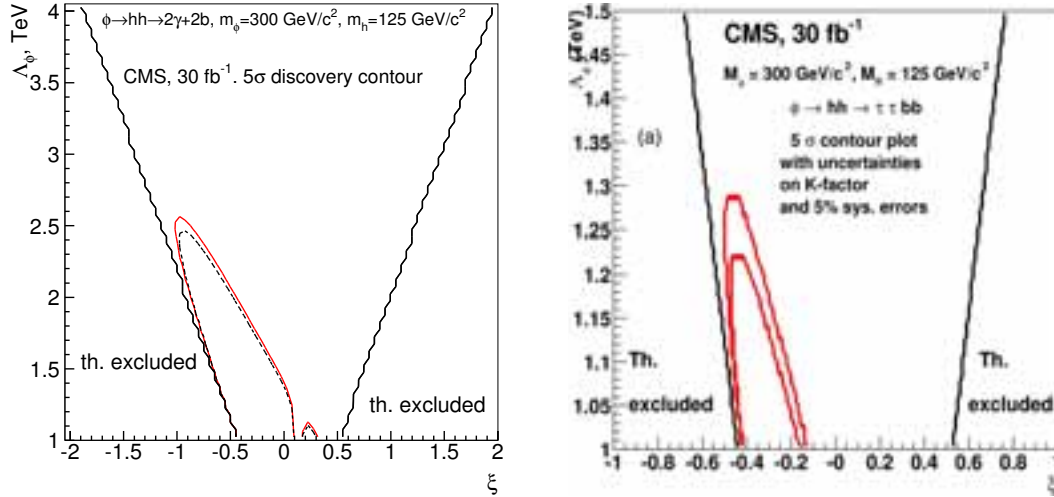
Fig. 9.13: Left plot: the 5σ discovery contours for the $\phi \rightarrow hh \rightarrow \gamma\gamma b\bar{b}$ channel for 30 fb^{-1}. The solid (dashed) contour shows the discovery region without (with) the effects of the systematic uncertainties (find more explanations in the text). Right plot: the 5σ discovery contours for the $\phi \rightarrow hh \rightarrow \tau\tau b\bar{b}$ channel for 30 fb^{-1}. The two contours corresponds to the variation of the background NLO cross sections due to the scale uncertainty. The 5% experimental systematics on the background is taken into account (see text).

signal-to-background ratio is always less than 10% before the mass cuts are applied. The final cuts on the $M_{\gamma\gamma}$, $M_{j\bar{b}}$ and $M_{\gamma\gamma b\bar{b}}$ introduce a systematic uncertainty on the number of the background events expected after these cuts. This uncertainty is determined by the following factors: the energy scale uncertainty for the photons and jets, and the theoretical uncertainty of the shape of the mass distributions due to the scale and PDF uncertainties. Figure 9.13 (left plot) shows the 5σ discovery contours for the $\phi \rightarrow hh \rightarrow \gamma\gamma b\bar{b}$ channel for 30 fb^{-1}. The solid (dashed) contour shows the discovery region without (with) the effects of the systematic uncertainties.

For the $\tau\tau b\bar{b}$ final state the background uncertainty due to the experimental selections was estimated to be between 5% and 10% [34]. Figure 9.13 (right plot) shows the 5σ discovery contours for the $\phi \rightarrow hh \rightarrow \tau\tau b\bar{b}$ channel for 30 fb^{-1}. The two contours correspond to the variation of the background NLO cross sections due to the scale uncertainty. The 5% experimental systematics on the background is taken into account.

9.5 Search for Randall-Sundrum excitations of gravitons decaying into two photons in CMS

Marie-Claude Lemaire, Vladimir Litvin and Harvey Newman

To test the Randall-Sundrum model, not only Higgs/radion but also graviton production needs to be studied. This contribution discusses the CMS discovery potential; full simulation and reconstruction are used to study diphoton decay of Randall-Sundrum gravitons. For an integrated luminosity of 30 fb^{-1} diphoton decays of Randall-Sundrum gravitons can be discovered at 5σ level for masses up to 1.61 TeV in case of weak coupling between graviton excitations and Standard Model particles $k/\bar{M}_{Pl} \equiv c$ ($c = 0.01$). Heavier resonances can be detected for larger coupling constant ($c = 0.1$), with mass reach of 3.95 TeV.

The search for the $G \rightarrow \gamma\gamma$ signal at LHC is affected by four types of backgrounds:

- The prompt di-photon production from the quark annihilation ("Born") and gluon fusion diagrams ("Box"), which provides an intrinsic or 'irreducible' background.
- The γ + jets ("Brem") production consisting of two parts: i) prompt photon from hard interaction + the second photon coming from the outgoing quark due to final state radiation and ii) prompt

photon from hard interaction + the decay of a neutral hadron (mostly isolated π^0) in a jet, which could fake a real photon.

– The background from QCD hadronic jets ("QCD"), where electromagnetic energy deposits result from the decay of neutral hadrons (especially isolated π^0s) in both jets.

– Drell Yan process with $e^+ e^-$ in a final state ("DY") which could mimic photons when correspondent electron tracks will not be assigned to the superclusters during the reconstruction.

The analysis was done as follows:

1 To find two super-clusters (SCs) with $E_T > 150$ GeV and two HLT trigger bits triggered at the same time: 1) 2p (two isolated photons with trasnverse energies larger than 40 GeV and 25 GeV respectively, without any other energy deposited in electromagnetic calorimeter within distance R ($R = \sqrt{\delta\eta^2 + \delta\phi^2}$) less than 0.5 from the photon); and 2) r2p (two photons with trasnverse energies larger than 40 GeV and 25 GeV respectively, without any isolation).

2 Calorimeter isolation criteria: for each SC the energy in a cone of $\Delta R = 0.5$ (excluding SC itself) should be $< 0.02 E_T(SC)$

3 $E(\text{HCAL})/E(\text{ECAL}) < 0.05$

4 Tracker isolation: the sum of the energy of all tracks in a cone $\Delta R = 0.5$ around the SC should be $< 0.01 E_T(SC)$

5 Photon energy corrections are done in a simple way so far:
  - If the crystal in SC with largest deposited energy had less than 1.7 TeV, only simple energy dependent part of correction is applied (just a shift of the peak)
  - If the crystal in SC with largest deposited energy had more than 1.7 TeV, the Multi-Gain-Pre-Amplifier (MGPA) saturation correction (1d) was applied

To produce the final results and to calculate the expected statistical significance for RS-1 graviton search recently calculated next-to-leading order corrections (K factors) to the cross sections of different types of background are used: K = 1.5 for quark annihilation [41], K = 1.2 for gluon fusion [42], K = 1 for the γ + hadronic jets [42] and K = 1 for QCD jets. For signal, a conservative K= 1 value is taken.

The graviton invariant mass is reconstructed from the two Super-Clusters. For each value of the generated graviton mass, the corresponding peak is fitted to a Gaussian distribution. The σ of the fit is $\simeq$ 10 GeV for M_G = 1.5 TeV and c=0.01, reflecting the detector energy resolution, which is slightly below 0.5% constant term, as obtained from 2004 test beam data; and an additional contribution of 0.16% which is due to the reconstruction. For M_G = 3.5 TeV and c=0.1 it increases up to $\simeq$ 35 GeV, due to the natural width of the resonance.

A $\pm 3\sigma$ window is defined around the fitted peak to compute the numbers of signal and background events, N_s and N_{bkg}. The corresponding number of events, obtained through the successive analysis cuts described above are given for an integrated luminosity 30 fb^{-1} in Table 9.2 for ($M_G = 1.5$ TeV, $c = 0.01$) and in Table 9.3 for ($M_G = 3.5$ TeV, $c = 0.1$).

Signals over backgrounds with all events satisfying all the selection cuts are displayed in Fig. 9.14 for ($M_G = 1.5$ TeV, $c = 0.01$), ($M_G = 3.0$ TeV, $c = 0.1$) and for an integrated luminosity of 30 fb^{-1}. In Fig. 9.15, signal over backgrounds are given for ($M_G = 1.0$ TeV, $c = 0.01$), ($M_G = 2.5$ TeV, $c = 0.1$) and for an integrated luminosity of 10 fb^{-1}.

Taking into account the K-factors described above, we have got next number of events for signal and background and calculated significance for $c = 0.01$ and $c = 0.1$, for the $L = 30$ fb^{-1}. $S = \sqrt{2lnQ}$, with $Q = (1 + n_s/n_b)^{n_s + n_b} exp(-n_s)$ in Tables 9.4 and 9.5.

Expected statistical significance S_{L2} is plotted for (M_G, c) space for 10, 30 and 60 fb^{-1} (Fig. 9.16). Uncertainties were not taken into account in Fig. 9.16.

The discovery region in the plane of the coupling parameter c and the graviton mass is given in Fig. 9.17.

Table 9.2: Number of events passed through the analysis cuts defined above for $M_G = 1.5$ TeV, $c = 0.01$ and $L = 30$ fb^{-1}. Leading column is non-saturated events, all saturated events, passed through the analysis, were added in brackets, where applied.

	Signal	Born (k=1.5)	Box (k=1.2)	Brem (k=1)	QCD (k=1)	DY (k=1)
trigger + 2SC	28.9	8.6	0.10	29.2	798.7	4.3
+ EM isolation	24.5	5.5	0.08	20.3	361.8	3.5
+ HCAL/ECAL	24.3	5.4	0.08	4.4	12.8	3.5
+ tracker isolation	17.6	4.2(+0.2)	0.05	0.17	0.0	0.0

Table 9.3: Number of events passed through the analysis cuts defined above for $M_G = 3.5$ TeV, $c = 0.1$ and $L = 30$ fb^{-1}. Leading column is non-saturated events, all saturated events, passed through the analysis, were added in brackets, where applied.

	Signal	Born (k=1.5)	Box (k=1.2)	Brem (k=1)	QCD (k=1)	DY (k=1)
trigger + 2SC	11.6	0.20	$4.4 * 10^{-4}$	0.78	821.9	0.10
+ EM isolation	10.8	0.14	$3.6 * 10^{-4}$	0.32	164.4	0.095
+ HCAL/ECAL	10.6	0.13	$3.4 * 10^{-4}$	0.016	0.0	0.095
+ tracker isolation	8.9(+1.0)	0.10(+0.02)	$2.7(+0.24) * 10^{-4}$	$1.7 * 10^{-3}$	0.0	$7.2 * 10^{-4}$

Table 9.4: Significance for $c = 0.01$ and $L = 30$ fb^{-1}

	$M_G = 1.0$ TeV	$M_G = 1.25$ TeV	$M_G = 1.5$ TeV	$M_G = 1.75$ TeV	$M_G = 2.0$ TeV
N_s	135.8	44.0	17.6	7.3	3.9
N_{bkg}	15.0	8.8	4.6	1.8	1.2
Significance	20.6	10.1	5.9	3.9	2.6

Table 9.5: Significance for $c = 0.1$ and $L = 30$ fb^{-1}

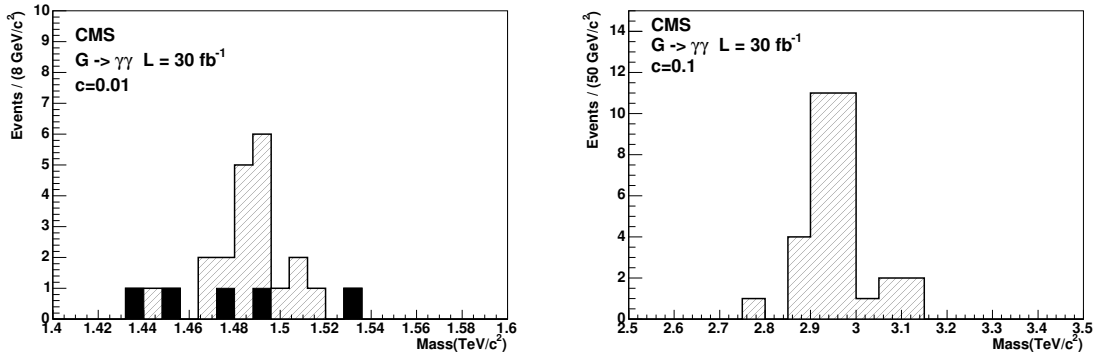|	$M_G = 2.5$ TeV	$M_G = 3.0$ TeV	$M_G = 3.5$ TeV	$M_G = 4.0$ TeV	$M_G = 4.5$ TeV
N_s	103.8	31.6	9.9	3.44	1.11
N_{bkg}	1.11	0.35	0.13	0.06	0.02
Significance	27.3	15.0	8.2	4.6	2.6

Fig. 9.14: Number of events passed through all cuts for (1.5 TeV, 0.01) (left) and (3.0 TeV, 0.1) (right) RS-1 gravitons for 30 fb^{-1} integrated luminosity.
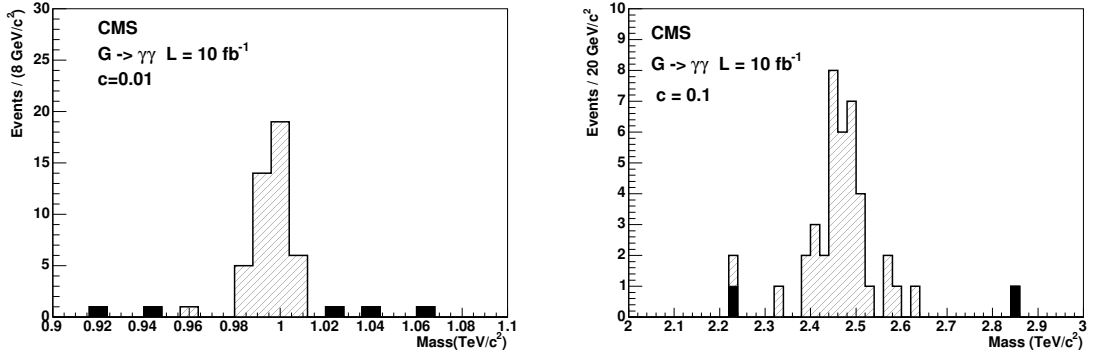

Fig. 9.15: Number of events passed through all cuts for (1.0 TeV, 0.01) (left) and (2.5 TeV,0.1) (right) RS-1 gravitons for 10 fb^{-1} integrated luminosity.

Recent results for 5σ discovery limits for 10, 30 and 60 fb^{-1} are presented in Table 9.6. Confidence limits uncertainties were calculated for 30 fb^{-1} and also presented in Table 9.6. The first uncertainty corresponds to hard scale uncertainties (it was varied from $0.25\hat{s}$ to $4\hat{s}$, default value was $\hat{s}$ of the subprocess). The second uncertainty corresponds to cross section uncertainties because of PDF uncertainties. The third uncertainty corresponds to the fact, that Tevatron most recent measures pointed out that Born K-factor might be closer to 2 [43] instead of 1.5 as was used in this study.

Table 9.6: Results for 5σ discovery limits for 10, 30 and 60 fb^{-1} and confidence limits uncertainties for 30 fb^{-1}

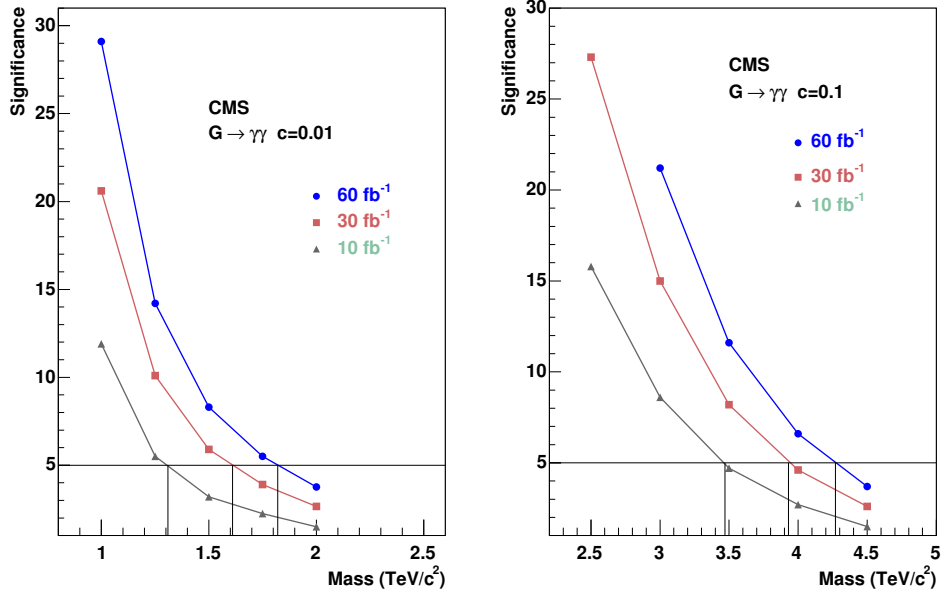|	for 60 fb^{-1}, GeV	for 30 fb^{-1}, GeV	for 10 fb^{-1}, GeV
$c = 0.01$	1820	$1610 + (+56 - 62) \pm 55 \pm 50$	1310
$c = 0.1$	4270	$3950 + (+42 - 47) \pm 152 \pm 30$	3470

Fig. 9.16: Significance as a function of the graviton mass for 10 fb^{-1} and 30 fb^{-1} integrated luminositiies, c=0.01 (left) and c=0.1 (right)
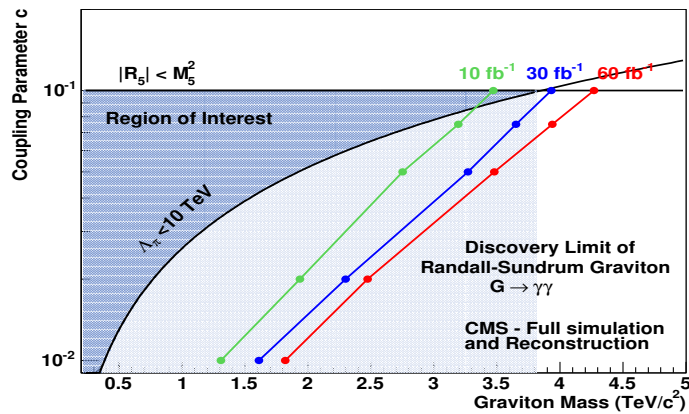

Fig. 9.17: Reach of the CMS experiment in the search for the Randall-Sundrum graviton decaying into diphoton channel as a function of the coupling parameter c and the graviton mass for 10 fb^{-1}, 30 fb^{-1} and 60 fb^{-1}. The left part of each curve is the region where the significance exceeds 5σ.

9.6 SUSY Higgs production from 5-D warped supergravity

Steve Fitzgerald

Scenarios which combine the five-dimensional warped spacetime of the Randall-Sundrum model [1, 44] with supersymmetry are interesting for a number of reasons. Firstly, they address the issue of radion stabilization – the energy scale at which SUSY is broken corresponds to the scale at which the scale-invariance of the Randall-Sundrum solution is broken, and hence sets the scale of the extra dimension; see for example [45–49]. Secondly, since they are derived from supergravity, the Giudice-Masiero mechanism [50] to resolve the μ-problem can be implemented. Thirdly, it seems possible to make contact with Type IIB string theory via a supersymmetric warped intermediate sector [51–54]. In this work, Higgs production in vector boson fusion is investigated, in the context of a minimal supersymmetric extension of the Standard Model realized on $\mathcal{M}_4 \times S_1/Z_2$. The model, [55], is inspired by 5-D $\mathcal{N} = 2$ supergravity. The $VV - H_i^0$ channel is sensitive to these scenarios, as it receives contributions both from corrections to the $VV - H_i^0$ vertex itself, and from new 4-point vertices appearing in the 4-D effective Lagrangian. Production cross-sections, k_T and rapidity distributions are calculated for a high-energy e^+e^- collider, and compared with those of the MSSM.

9.6.1 The model

The model under consideration first appeared in [55]. Starting from 5-D, $\mathcal{N} = 2$ supergravity realized on $\mathcal{M}_4 \otimes S_1/Z_2$, constant brane energy densities are added at the Z_2 fixed points. The 5-D Einstein equations then admit the Randall-Sundrum solution

$$ds^2 = e^{-2kr_c\phi}\eta_{\mu\nu}dx^\mu dx^\nu - r_c^2 d\phi^2 \tag{9.22}$$

and the 5-D, $\mathcal{N} = 2$ SUSY in bulk is broken to 4-D, $\mathcal{N} = 1$ on the brane by the localized energy densities and orbifold projection. If we give the modulus field for the fifth dimension (T) a VEV:

$$\langle T + T^\dagger \rangle = \log\left[\frac{3M_p^2}{\Lambda^2}\right]; \quad T = \langle T \rangle + \frac{t}{\Lambda} \tag{9.23}$$

we can extract the 4-D effective theory on the brane fixed at $\phi = \pi$, and arrive at a theory which looks like the MSSM with some important differences. In the equation above, M_P is the unwarped 4-D Planck mass, related to the 5-D Planck mass via $kM_P^2 = M_5^3$; Λ and t are defined below.

We use the standard MSSM superpotential with μ-term modified (see later):

$$\begin{aligned} W &= h_U^{ij}Q_{Li} \cdot H_2 U_{Rj} + h_D^{ij}H_1 \cdot Q_{Li}D_{Rj} \\ &+ h_E^{ij}H_1 \cdot L_{Li}E_{Rj} + \mu H_1 \cdot H_2. \end{aligned} \tag{9.24}$$

A non-minimal effective Kähler potential K_{eff} is obtained by integrating the action over the compactified dimension and comparing the curvature term with 4-D SUGRA. This is due to the fact that we are trying to match an effective theory defined on a flat 4-D spacetime with a higher-dimensional bulk which is curved. This necessitates some important field redefinitions which result in an additional level of mixing (see later).

$$K_{\text{eff}} = \Lambda^2 \exp\left\{-\frac{t+t^*}{\Lambda} + \frac{1}{\Lambda^2}\sum_i |\phi_i|^2 + (\lambda H_1 \cdot H_2 + \text{h.c.})\right\} \tag{9.25}$$

In the above expression, Λ represents the cutoff for the effective theory, ϕ_i represents all matter + Higgs scalars, and λ is a parameter allowing "chiral" Higgs terms in K ("·" = $SU(2)$ product $H_1 \cdot H_2 = H_1^0 H_2^0 - H_1^- H_2^+$). There also arises an extra neutral scalar t – the *radion*, which can mix with the neutral

Higgses, and its fermionic partner χ_t, the *radino*, which can mix with the neutral gauginos and Higgsinos, resulting in five neutralinos, compared with four in the MSSM. λ contributes to the μ-parameter in the superpotential:

$$\mu = \mu_0 + \lambda m_{3/2}, \tag{9.26}$$

via the Giudice-Masiero mechanism. One can remove μ_0 entirely, so $\mu \sim m_{3/2}$, or leave it in at $\mathcal{O}(M_P)$, naturally warped down to $\mathcal{O}(\Lambda)$. The 'free' parameters Λ, λ, μ_0, and $m_{3/2}$ are constrained by electroweak symmetry breaking (EWSB) as follows [55]:

$$\lambda \sim \frac{-1}{3 + \sqrt{3}} \left\{ 1 - (1 + \sqrt{3}) \frac{\mu}{m_{3/2}} + \frac{\mu^2}{m_{3/2}^2} \right\}. \tag{9.27}$$

The MSSM parameter $\tan\beta = 1$ after EWSB.

The scalar kinetic terms in the effective Lagrangian

$$\sim \frac{\partial^2 K}{\partial\phi_I \partial\phi_J^*} D_\mu \phi_I D^\mu \phi_J \equiv K_{IJ} D_\mu \phi_I D^\mu \phi_J, \tag{9.28}$$

where K_{IJ} is the *Kähler metric*. For a minimal $K = \sum_i |\phi_i|^2$, $K_{IJ} = \delta_{IJ}$, and the usual structure is recovered. However, a non-minimal K leads to a non-diagonal K_{IJ} and what is known as *kinetic mixing* of the scalar fields, when one performs the field redefinition to return the kinetic terms to canonical form. The effect is least suppressed in the neutral scalar and neutralino sector.

These (holomorphic) transformations take the form (to $\mathcal{O}(1/\Lambda)$):

$$\begin{pmatrix} H_1^0 \\ H_2^0 \\ t \end{pmatrix} \longrightarrow \begin{pmatrix} 1 & 0 & \frac{1+\lambda}{4}\frac{v}{\Lambda} \\ 0 & 1 & \frac{1+\lambda}{4}\frac{v}{\Lambda} \\ \frac{1+\lambda}{4}\frac{v}{\Lambda} & \frac{1+\lambda}{4}\frac{v}{\Lambda} & 1 \end{pmatrix} \begin{pmatrix} H_1^0 \\ H_2^0 \\ t \end{pmatrix} \tag{9.29}$$

diagonalizing kinetic terms and rescaling fields. There are two levels of mixing: the above plus the normal weak mixing of neutral degrees of freedom. This leads to (CP-even scalar) mass matrix

$$M^2 = \begin{pmatrix} A + B/\Lambda^2 & 0 & 0 \\ 0 & C/\Lambda^2 & D/\Lambda \\ 0 & D/\Lambda & E + F/\Lambda^2 \end{pmatrix} \tag{9.30}$$

with A to F depending on other scales in the theory, v, $m_{3/2}$, μ (Appendix C of [55]). The first scalar is still an exact eigenstate – there is no 1–2, 1–3 mixing. As $\Lambda \to \infty$, $\tan\beta \to 1$, i.e. a D-flat direction in this limit. The finite-Λ corrections break the D-flatness. Also, the lightest Higgs can be up to ~ 700 GeV without violating the LEP bounds. Figure 9.18 shows the mass of the lightest scalar vs. μ for various values of Λ. One finds an an *upper* bound of $\Lambda \sim 4.4$–9.5 TeV from $m_H > 114$ GeV (from breaking of D-flatness by Λ-suppressed terms).

9.6.2   SUSY Higgs production in W^+W^- fusion

We now consider the process $e^+ e^- \longrightarrow \nu\bar{\nu}H_0$. Below are the SM/MSSM tree-level diagrams:
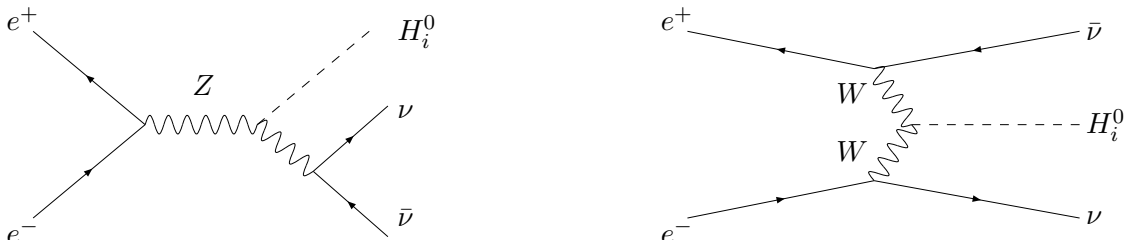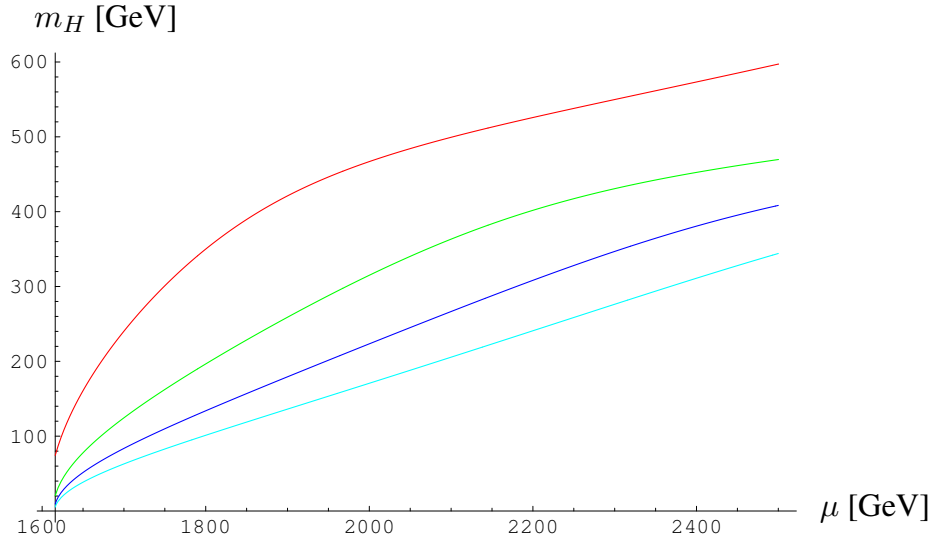
Fig. 9.18: The mass of the lightest scalar as a function of μ for (top to bottom) $\Lambda = 2, 4, 6, 8$ TeV.

We can safely neglect the Higgsstrahlung diagram at high $\sqrt{s}$, as t-channel $\ln s$ growth dominates, and we also neglect diagrams with Higgs radiation off e^+, e^-, due to the small Yukawas. New and modified vertices appear in the 4-D effective interaction Lagrangian: the WWH vertex is modified and a new adjacency 4 vertex arises (with associated Feynman rules in Eq. (9.31)):
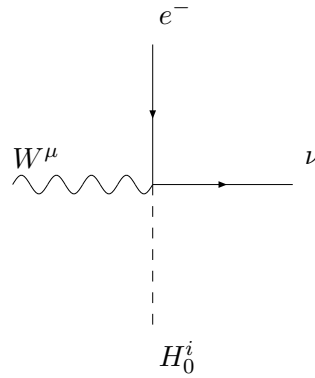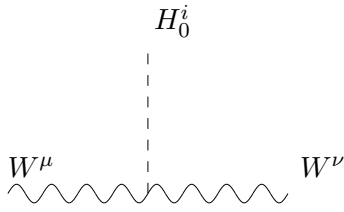
$$\frac{ie^2}{2\sin^2\theta_W}\left\{v(Z_R^{1i} + Z_R^{2i}) + \frac{1 - 2\sqrt{2} + \lambda}{2}\frac{v^2}{\Lambda}Z_R^{3i}\right\}g^{\mu\nu}; \quad \frac{ie}{\Lambda\sin\theta_W}\gamma^\mu P_L Z_R^{3i}. \qquad (9.31)$$
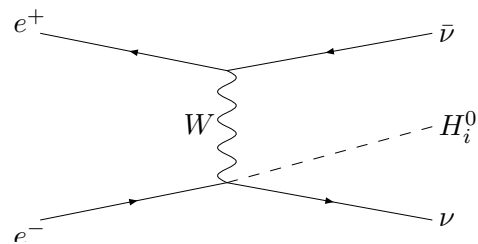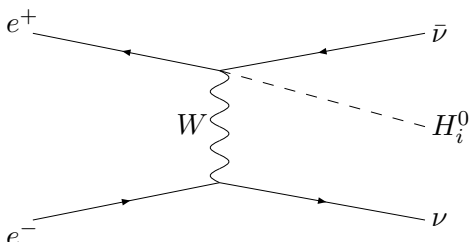
The following new diagrams appear:

402

Table 9.7: Parameters of points used

	Point 1	Point 2	Point 3	MSSM	SM
Λ (GeV)	4000	4000	8000	N/A	N/A
$m_{3/2}$ (GeV)	500	350	500	N/A	N/A
$R_1 + R_2$	0.97	0.96	0.99	0.90	0
R_3	$-8D - 7$	$-1.9D - 6$	$-5.5D - 7$	0	0
μ (GeV)	1695	1234	1853	1850	N/A

The extra ($\frac{1}{\Lambda}$-suppressed) diagrams come from the following structure in the effective Lagrangian:

$$\mathcal{L} \sim \left(1 - \frac{t + t^*}{\Lambda}\right) \times \mathcal{L}_{\text{MSSM}}^{\text{kinetic}} \tag{9.32}$$

Also, the contribution from term $(1/\Lambda)\bar{\chi}_t\sigma^\mu\chi_t\partial_\mu t$ gives a correction to Yukawas, and hence the following diagrams appear:
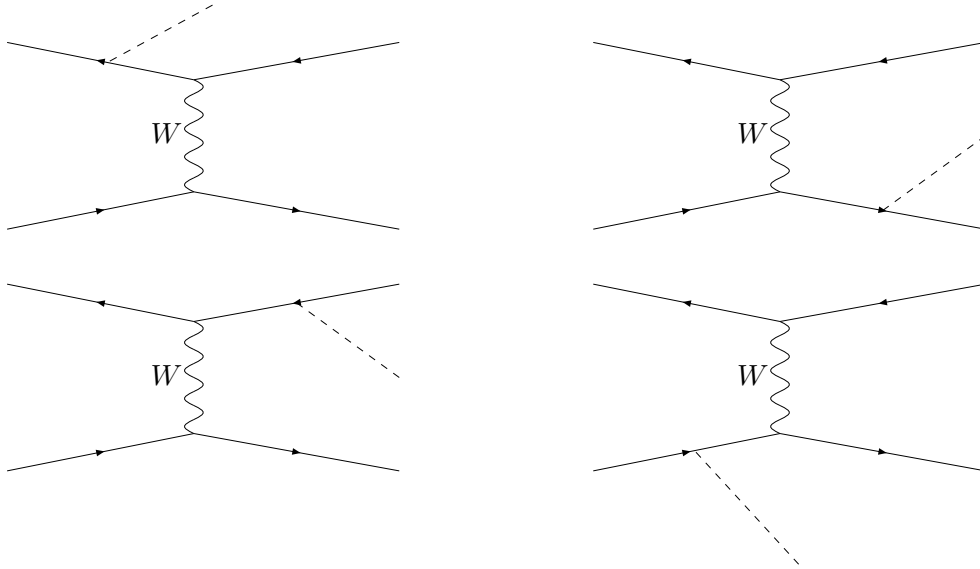
However, their contributions cancel exactly in the matrix element. Any potentially large effects on the decays, say, $\sqrt{s}/\Lambda$, say, cancel, leaving observables unaffected to $\mathcal{O}(m_f/\Lambda)$. We parameterize the matrix element as

$$|\mathcal{M}|^2 = |\mathcal{M}_{SM}|^2\{R_1 + R_2 + R_3(p_1 \cdot p_1' + p_2 \cdot p_2' + m_W^2)\}, \tag{9.33}$$

where:

– R_1 : like $\sin^2(\beta - \alpha)$ in MSSM.
– R_2 : Correction to WWH vertex.
– R_3 : Contribution from new diagrams.

The dominant effect arises from the WWH vertex modification (see Table 9.7). Can it be distinguished from normal mSUGRA? We choose a Higgs mass of 120 GeV (we assume it is known from LHC). The mixing matrices, and hence the normalization of the cross-section, will differ from that of mSUGRA. Table 9.7 gives the parameters of the points chosen for comparison. The mSUGRA point used has lightest scalar at 120 GeV and $\tan\beta = 3$, (from using the low energy mass matrix, β, m_A, m_Z in the standard way).
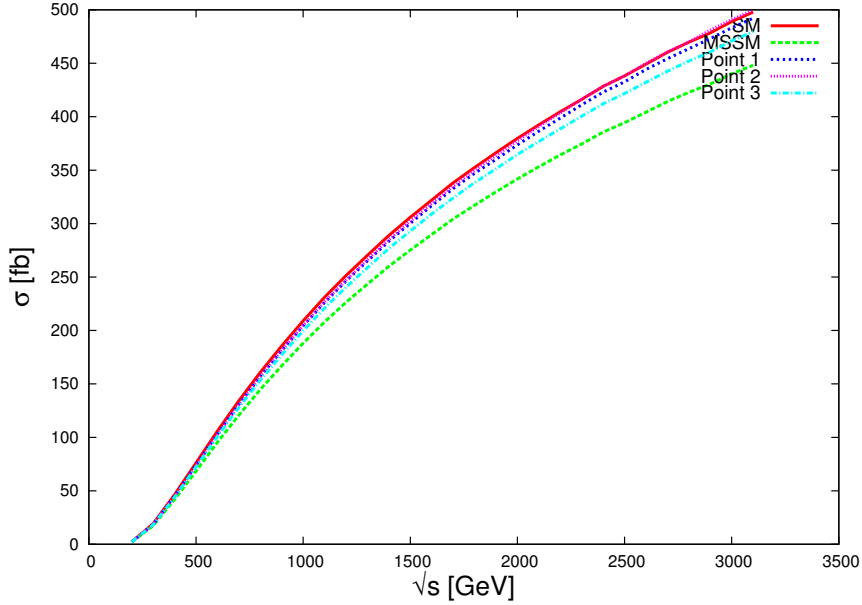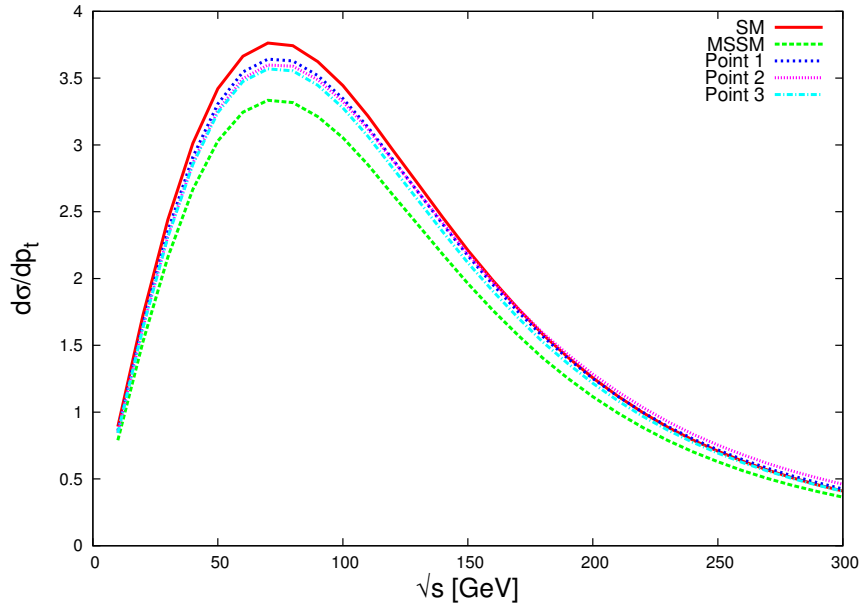
Fig. 9.19: Total cross sections for the points of Table 9.7.

Fig. 9.20: p_T distributions for the points of Table 9.7.

It should be noted that these example points above represent a 'worst case scenario,' where the model would be most difficult to distinguish from the closest mSUGRA point, and indeed in this scenario it would be difficult, as the differences are only about 10%. This is illustrated in Figs. 9.19 and 9.20, where the cross sections and p_T distributions for the example points are plotted against $\sqrt{s}$. A more likely scenario would be an unusually heavy lightest scalar, which could be satisfactorily explained by a scenario like the one under consideration. Having a cutoff for an effective theory in the TeV region necessarily makes phenomenological effects small, and a linear collider would be indispensable in distinguishing this model from other SUSY scenarios.

REFERENCES

[1] L. Randall and R. Sundrum, Phys. Rev. Lett. **83**, 3370 (1999), [hep-ph/9905221].

[2] H. Davoudiasl, J. L. Hewett and T. G. Rizzo, Phys. Rev. Lett. **84**, 2080 (2000), [hep-ph/9909255].

[3] H. Davoudiasl, J. L. Hewett and T. G. Rizzo, Phys. Rev. **D63**, 075004 (2001), [hep-ph/0006041].

[4] W. D. Goldberger and M. B. Wise, Phys. Rev. Lett. **83**, 4922 (1999), [hep-ph/9907447].

[5] H. Davoudiasl, J. L. Hewett and T. G. Rizzo, Phys. Lett. **B473**, 43 (2000), [hep-ph/9911262].

[6] A. Pomarol, Phys. Lett. **B486**, 153 (2000), [hep-ph/9911294].

[7] Y. Grossman and M. Neubert, Phys. Lett. **B474**, 361 (2000), [hep-ph/9912408].

[8] T. Gherghetta and A. Pomarol, Nucl. Phys. **B586**, 141 (2000), [hep-ph/0003129].

[9] M. Carena, T. M. P. Tait and C. E. M. Wagner, Acta Phys. Polon. **B33**, 2355 (2002), [hep-ph/0207056].

[10] H. Davoudiasl, J. L. Hewett and T. G. Rizzo, JHEP **08**, 034 (2003), [hep-ph/0305086].

[11] H. Davoudiasl, J. L. Hewett and T. G. Rizzo, Phys. Rev. **D68**, 045002 (2003), [hep-ph/0212279].

[12] M. Carena, E. Ponton, T. M. P. Tait and C. E. M. Wagner, Phys. Rev. **D67**, 096006 (2003), [hep-ph/0212307].

[13] F. del Aguila, M. Perez-Victoria and J. Santiago, JHEP **02**, 051 (2003), [hep-th/0302023].

[14] F. del Aguila, M. Perez-Victoria and J. Santiago, hep-ph/0305119.

[15] F. del Aguila, M. Perez-Victoria and J. Santiago, Acta Phys. Polon. **B34**, 5511 (2003), [hep-ph/0310353].

[16] H. Davoudiasl, B. Lillie and T. G. Rizzo, hep-ph/0508279.

[17] H. Davoudiasl, B. Lillie and T. G. Rizzo, hep-ph/0509160.

[18] B. C. Allanach, K. Odagiri, M. A. Parker and B. R. Webber, JHEP **09**, 019 (2000), [hep-ph/0006114].

[19] H. Davoudiasl, J. L. Hewett and T. G. Rizzo, JHEP **04**, 001 (2003), [hep-ph/0211377].

[20] T. G. Rizzo, JHEP **01**, 028 (2005), [hep-ph/0412087].

[21] G. F. Giudice, R. Rattazzi and J. D. Wells, Nucl. Phys. **B595**, 250 (2001), [hep-ph/0002178].

[22] C. Csaki, M. L. Graesser and G. D. Kribs, Phys. Rev. **D63**, 065002 (2001), [hep-th/0008151].

[23] J. L. Hewett and T. G. Rizzo, JHEP **08**, 028 (2003), [hep-ph/0202155].

[24] D. Dominici, B. Grzadkowski, J. F. Gunion and M. Toharia, Acta Phys. Polon. **B33**, 2507 (2002), [hep-ph/0206197].

[25] D. Dominici, B. Grzadkowski, J. F. Gunion and M. Toharia, Nucl. Phys. **B671**, 243 (2003), [hep-ph/0206192].

[26] J. F. Gunion, H. E. Haber, G. L. Kane and S. Dawson, SCIPP-89/13.

[27] M. Chaichian, A. Datta, K. Huitu and Z.-h. Yu, Phys. Lett. **B524**, 161 (2002), [hep-ph/0110035].

[28] A. Djouadi, J. Kalinowski and M. Spira, Comput. Phys. Commun. **108**, 56 (1998), [hep-ph/9704448].

[29] M. Battaglia, S. De Curtis, A. De Roeck, D. Dominici and J. F. Gunion, Phys. Lett. **B568**, 92 (2003), [hep-ph/0304245].

[30] S. Abdullin *et al.*, Eur. Phys. J. **C39S2**, 41 (2005).

[31] G. Azuelos, D. Cavalli, H. Przysiezniak and L. Vacavant, The Beyond the Standard Model Working Group: summary report, Workshop on Physics at TeV Colliders, Les Houches, France, 2001, [hep-ph/0204031].

[32] D. Dominici, G. Dewhirst, S. Gennai, L. Fano and A. Nikitenko, Prepared for Lake Louise Winter Institute 2004 on Fundamental Interactions (LL WI 2004), Lake Louise, Alberta, Canada, 15–21 Feb 2004.

[33] K. Desch and M. Battaglia, Prepared for 5th International Linear Collider Workshop (LCWS 2000), Fermilab, Batavia, Illinois, 24–28 Oct 2000.

[34] D. Dominici, G. Dewhirst, A. Nikitenko, S. Gennai and L. Fanò, CMS Note 2005/007 (2005).

[35] G. Azuelos, D. Cavalli, H. Przysiezniak and L. Vacavant, Eur. Phys. J. direct **C4**, 16 (2002).

[36] T. G. Rizzo, JHEP **06**, 056 (2002), [hep-ph/0205242].

[37] ATLAS Collaboration, ATLAS detector and physics performance. Technical design report. Vol. 2, CERN-LHCC-99-15.

[38] T. Sjostrand *et al.*, Comput. Phys. Commun. **135**, 238 (2001), [hep-ph/0010017].

[39] E. Richter-Was, D. Froidevaux and L. Poggioli, ATLFAS 2.0 a fast simulation package for ATLAS, ATL-PHYS-98-131.

[40] B. A. Mohn, An ATLAS simulation study of Higgs and radions in the $\mathrm{h}(\phi) \to zz4\ell$ channels, Cand. Scient. thesis, University of Bergen, 2003.

[41] W. Giele *et al.*, hep-ph/0204316.

[42] Z. Bern, L. J. Dixon and C. Schmidt, Phys. Rev. **D66**, 074018 (2002), [hep-ph/0206194].

[43] D. Acosta *et al.* (CDF Collaboration), Phys. Rev. Lett. **95**, 022003 (2005).

[44] L. Randall and R. Sundrum, Phys. Rev. Lett. **83**, 4690 (1999), [hep-th/9906064].

[45] M. Redi, hep-ph/0402195.

[46] G. von Gersdorff, M. Quiros and A. Riotto, Nucl. Phys. **B689**, 76 (2004), [hep-th/0310190].

[47] A. Delgado, G. von Gersdorff and M. Quiros, JHEP **12**, 002 (2002), [hep-th/0210181].

[48] N. Maru and N. Okada, Phys. Rev. **D70**, 025002 (2004), [hep-th/0312148].

[49] M. Eto, N. Maru and N. Sakai, Phys. Rev. **D70**, 086002 (2004), [hep-th/0403009].

[50] G. F. Giudice and A. Masiero, Phys. Lett. **B206**, 480 (1988).

[51] M. J. Duff, J. T. Liu and K. S. Stelle, J. Math. Phys. **42**, 3027 (2001), [hep-th/0007120].

[52] R. Arnowitt, J. Dent and B. Dutta, Phys. Rev. **D70**, 126001 (2004), [hep-th/0405050].

[53] P. Horava and E. Witten, Nucl. Phys. **B475**, 94 (1996), [hep-th/9603142].

[54] P. Horava and E. Witten, Nucl. Phys. **B460**, 506 (1996), [hep-th/9510209].

[55] J. A. Casas, J. R. Espinosa and I. Navarro, Nucl. Phys. **B620**, 195 (2002), [hep-ph/0109127].